

FIG. 3. Variation of the apparent conductivity  $\sigma_{ij}$  normalized by the film conductivity  $\sigma_F$  with j for a conductor-core particle.

$$\sigma_{Ij} = \frac{1 - \zeta^3}{1 + (1/2)\zeta^3} \sigma_F < \sigma_F$$
 for the perfect-dielectric core. (27)

With increasing j,  $\sigma_{Ij}$  becomes lower for the conductor-core particle but higher for the dielectric-core particle. Figures 3 and 4 display the variation of  $\sigma_{Ij}$  for the conductor-core and dielectric-core particles, respectively. The figures indicate that, when j is sufficiently high, the conductivity approximates  $\sigma_F$ , independent of the core type. This means that any effect of the core vanishes at a high j. It can also be seen from the figures that  $\sigma_{Ij}$  of the particle having a thinner film converges to  $\sigma_F$  at a larger j and gives a wider range of  $\sigma_{Ij}$ .

Another implication by Figs. 3 and 4 is that, at low values of j,  $\sigma_{lj}$  of the conductor-core ( $\sigma_C = \infty$ ) and dielectric-core ( $\sigma_C = 0$ ) particles are characterized by the  $\sigma_F/t$  and  $\sigma_F t$ , respectively. (Needless to say that if  $\sigma_C = \sigma_F$ , then  $\sigma_{lj} = \sigma_F$ , irrespective of t and j.) In a numerical field calculation, a thin surface film presents difficulty to realize the high accuracy if the film thickness is very small compared with the surface area. An approach often used to solve this problem is to treat the film as zero-thickness elements and introduce the surface conductivity, defined as  $\sigma_s = \sigma_F t$ , to be the calculation

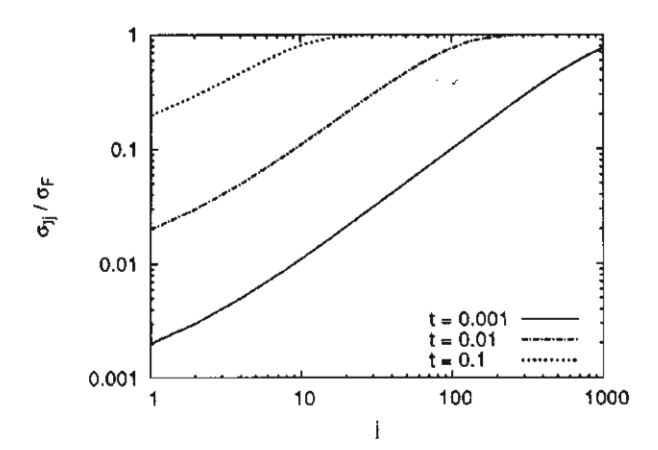


FIG. 4. Variation of the apparent conductivity  $\sigma_{Ij}$  normalized by the film conductivity  $\sigma_F$  with j for a dielectric-core particle.

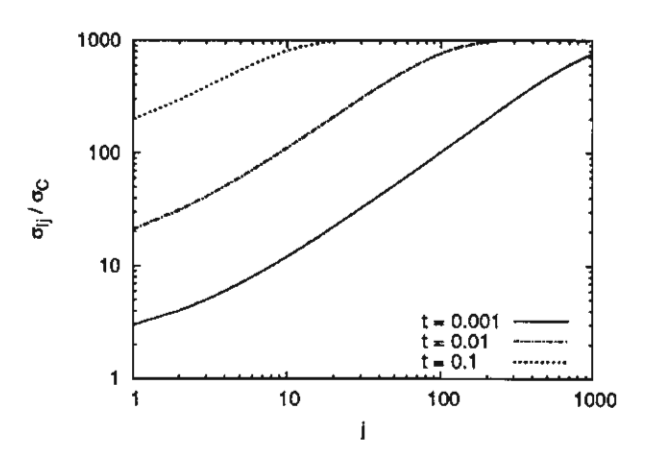


FIG. 5. Variation of the apparent conductivity  $\sigma_{Ij}$  normalized by the core conductivity  $\sigma_{C}$  of the conductive-core particle for  $\Gamma_{FC}$ =1000.

parameter. Our analysis, however, shows that the approximation to zero-thickness surface elements is appropriate only where the film conductivity is predominant over the core one. However, even for the dielectric-core particle,  $\sigma_{Ij}$  corresponding to a high (j-1)th-order external field is approximately equal to  $\sigma_E$ , no longer a function of  $\sigma_E t$ .

Figures 5 and 6 present  $\sigma_{Ij}$  for the general case that the particle core has a finite but nonzero conductivity. Figure 5 shows the variation of  $\sigma_{Ij}/\sigma_C$  of the particles having different film thickness as  $(\Gamma_{FC}=1000)$ . In the figure,  $\sigma_{Ij}$  varies from  $\sigma_{I1}$  given by Eq. (25) at j=1 to  $\sigma_F$  at a high j. The values of  $\sigma_{Ij}$  are always between the  $\sigma_C$  and the  $\sigma_F$ . With the thinner film, the particle gives the lower value of  $\sigma_{I1}$ , and  $\sigma_{Ij}$  more slowly converges to  $\sigma_F$ .

Figure 6 compares  $\sigma_{Ij}/\sigma_C$  between the particles that have different film thicknesses t but have the same value of  $\sigma_s/\sigma_C$ , where  $\sigma_s=\sigma_F t$  ( $\sigma_s/\sigma_C=1$  m). If the core conductivity is constant, it is evident from the figure that  $\sigma_{Ij}$  is approximately the same for all the particles at low values of j. However, at a higher j, the values of  $\sigma_{Ij}$  gradually deviate from each other. The deviation starting at a lower j for a thicker film reflects that particles of the same surface conductivity respond differently to an external electric field.

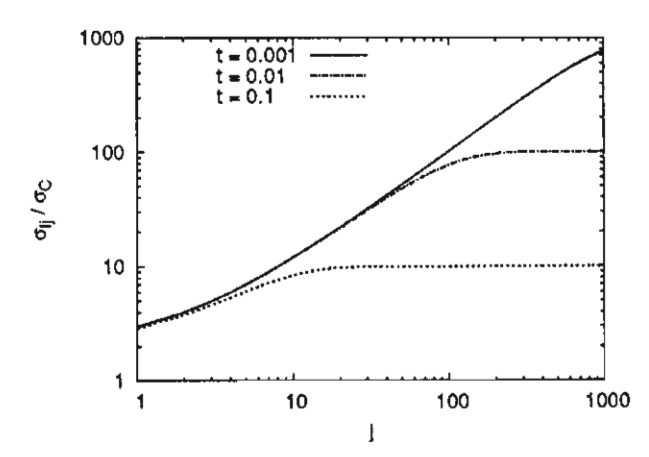


FIG. 6. Variation of the apparent conductivity  $\sigma_{IJ}$  normalized by the core conductivity  $\sigma_C$  of the conductive-core particle for a fixed  $\sigma_S/\sigma_C$ , where  $\sigma_S$  is the surface conductiviy.

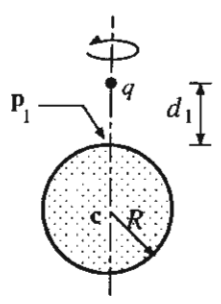


FIG. 7. Spherical particle and a point charge,

Thereby, the propriety of the film representation by  $\sigma_S$  depends not only on the film thickness and conductivity but also on the (i-1)th-order of the external field.

## IV. COMPARISON OF THE ELECTRIC FIELD AND FORCE

We have calculated two arrangements of particles to demonstrate the effects of the surface film on the electric field and dielectrophoretic force. The first arrangement is a spherical particle located at a distance  $d_1$  from a point charge q as shown in Fig. 7. The second arrangement is of two spherical particles spaced by a distance  $d_2$  under a uniform electric field  $E_2$  in the direction shown in Fig. 8. The former arrangement is used to investigate the fundamental response of the particle to a nonuniform field, which is, in this case, the electric field from the point charge. The interaction in the latter arrangement is more complicated than that in the former one, as the external field for each particle is the sum of  $E_2$  as well as the field due to the dipoles and higher-order multipoles induced in the other particle. We set the particle radius R to a unit length of 1 m, while varying  $d_1$  and  $d_2$  in the calculation.

For each arrangement, we have carried out the calculation for the three particle conditions: The homogeneous particle without a surface film, the conductor-core particle, and the dielectric-core particle. The homogeneous particles are assumed to have a conductivity  $\sigma_I = 10\sigma_E$ . We consider the film thickness t between 0.001R and 0.02R for the conductor-core and dielectric-core particles. This is the practical range for particles with their radius in the order of millimeter to micrometer. For each pair of the particle core and

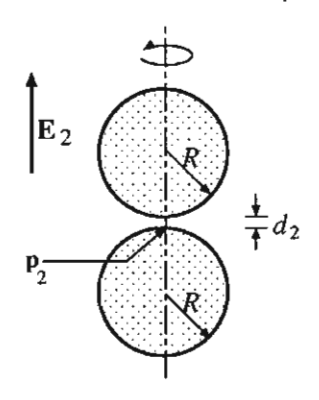


FIG. 8. Two spherical particles under a uniform field  $E_2$ .

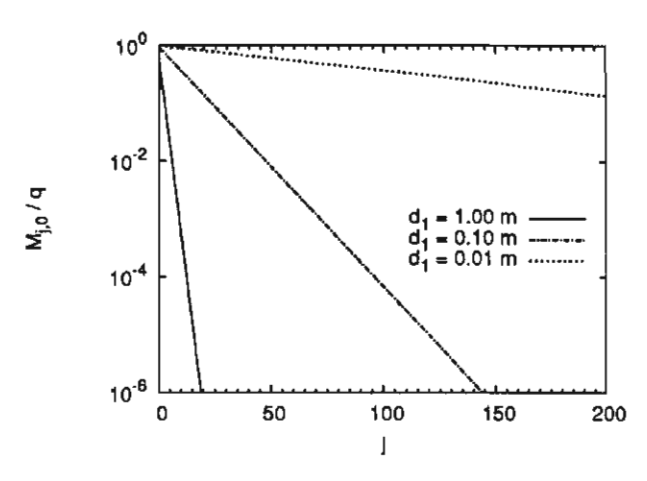


FIG. 9. Magnitude of the potential coefficient  $M_{j,0}$  in Eq. (1) for j = 0-200.

film thickness, we determine the value of  $\sigma_F$  in order that  $\sigma_{I1} = \sigma_I = 10\sigma_E$ . Thus, all the particles shall exhibit the same interaction with a uniform external field.

We have calculated the electric field on the particles by the method of multipole images using the multipole reexpansion technique. Equations (5), (6), (10)–(12), and (16)–(18) are utilized as the fundamental solutions of images for their corresponding particle types. We focus on the maximal electric field and force on the particle surface. The maximal electric field occurs at  $p_1$  in the first arrangement and  $p_2$  in the second arrangement. Note that, by the axisymmetry of the arrangements, we can simplify the expressions of the potentials, as explained in Sec. II

## A. A spherical particle and a point charge

The calculation results are shown in Figs. 9–11. Figure 9 displays the values of the expansion coefficient  $M_{j,0}$  in Eq. (1) when the point-charge potential is re-expanded about c for a different  $d_1$ . ( $M_{j,k}=0$  for  $k\neq 0$  because of the axisymmetry.) It is evident from Fig. 9 that  $M_{j,0}$  decreases rapidly with increasing j for the large  $d_1$ . When the separation  $d_1$ 

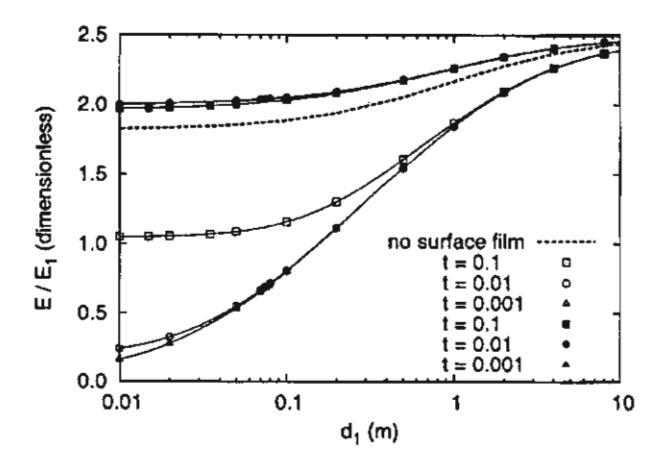


FIG. 10. Electric-field ratio at the point  $p_1$  of the arrangement in Fig. 7 as a function of  $d_1$ . The symbols  $\Box, \triangle$ , and  $\bigcirc$  represent the conductor-core particles, whereas  $\blacksquare$ ,  $\blacktriangle$ , and  $\bullet$  represent the dielectric-core particles.

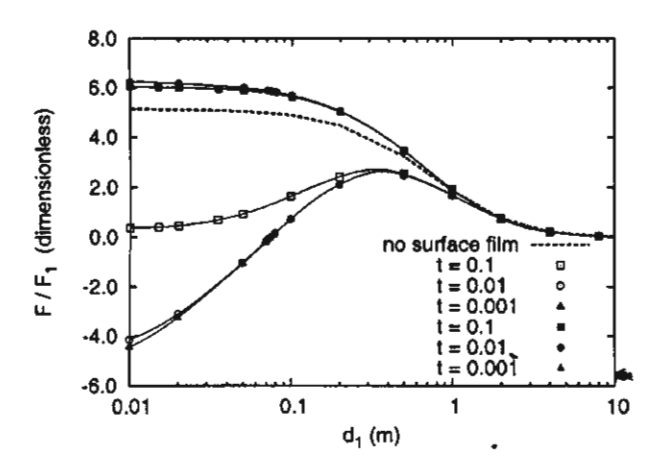


FIG. 11. Ratio of the force on the particle in Fig. 7 to  $F_1$ . The symbols  $\square$ ,  $\triangle$ , and  $\bigcirc$  represent the conductor-core particles, whereas  $\blacksquare$ ,  $\blacktriangle$ , and  $\bullet$  represent the dielectric-core particles.

becomes smaller, the external potential (and so the external field) due to q comprises the higher-order components, which cannot be neglected.

Figure 10 shows the electric field at  $p_1$  as a function of  $d_1$ . The field is presented as its ratio to  $E_1 = q/(4\pi d_1^2)$ , the field strength at  $p_1$  in the absence of the particle. It can be seen from Fig. 10 that, if  $d_1$  is sufficiently large, all the particles almost have the same magnitude of electric field. With decreasing  $d_1$ , the dielectric-core particle gives a higher electric field, whereas the conductor-core particle gives a lower electric field than the particle without a surface film. The effect of the film thickness also differs between the core types. The maximal field on the conductor-core particle of a smaller t/R is higher but vice versa on the dielectric-core particle. However, the variation of  $E/E_1$  becomes smaller as the thickness ratio decreases. Particularly, the difference between the t/R = 0.01 and 0.001 of the dielectric-core particle is hardly noticeable in Fig. 10. Note that, at small  $d_1$ , E is lower than  $E_1$  for the conductor-core particle with t/R=0.01 and 0.001.

Figure 11 presents the variation with the separation  $d_1$  of the dielectrophoretic force induced on the particles by the charge q. Similarly to the electric field, the force is shown by its ratio to  $F_1 = \frac{1}{2} \varepsilon_E E_1^2 R^2$ , where  $\epsilon_E$  is the permittivity of the surrounding medium. We have computed the force by integrating the Maxwell's stress over the particle surface.<sup>22</sup> (Alternatively, the force may be determined as the force acting on the charge q.) For a particle of an arbitrary radius, the force can be calculated from the values at the corresponding  $d_1$  in Fig. 11 and the normalizing factor  $F_1$ . Figure 11 shows that the force behavior is significantly different, depending on the core types. As d1 decreases, the attractive force induced on the dielectric-core particle gradually becomes stronger than the particle without a surface film. By contrast, the conductor-core particle shows a rather complex variation with  $d_1$ . With decreasing  $d_1$ , the force ratio initially increases, but after reaching the peak value, the force ratio decreases. If the film is thin enough, we can see that the force becomes repulsive at small  $d_1$ , e.g., at the separation closer than about 0.07 m for t/R=0.01 and 0.001 in the figure.

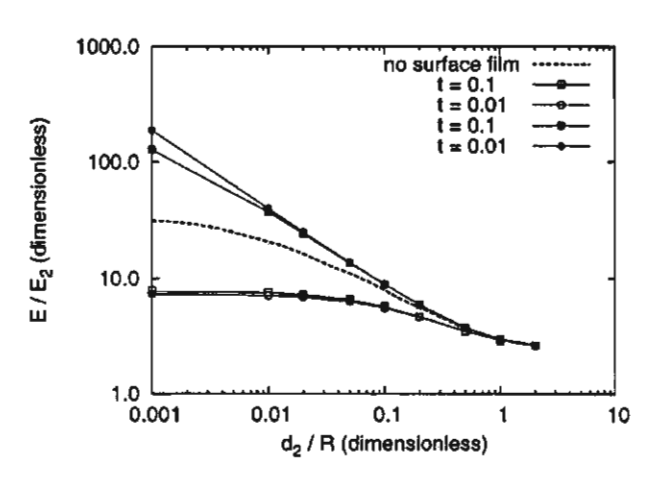


FIG. 12. Electric field at the point  $p_2$  of the arrangement in Fig. 8. The symbols  $\square$  and  $\bigcirc$  represent the conductor-core particles, whereas  $\blacksquare$  and  $\bigcirc$  represent the dielectric-core particles.

### B. Two spherical particles under a uniform field

In this arrangement, the electric field on each particle is intensified by the particle itself and by the existence of the other particle. Figure 12 shows the normalized electric field at  $p_2$ , as the functions of  $d_2$ . It can be seen that the decrease of  $d_2$  results in the field enhancement on all the particles. Similarly to the previous section, the electric field is lower on the conductor-core particle but higher on the dielectric-core particle compared with the particle without a surface film. The reduction of the film thickness moderates the field on the conductor-core particle but intensifies the field on the dielectric-core particle. Note that the electric field for t/R = 0.001 is omitted from the figure as it is very close to that for t/R = 0.01.

Figure 13 compares the dielectrophoretic forces on the particles at a different gap  $d_2$ . The force becomes stronger with decreasing  $d_2$  for all the particles. Compared with the particle without a surface film, the tendencies of the force on the particles are in the similar manner to those of the electric field shown in Fig. 12. The force in this arrangement is always attractive, inclined to reduce  $d_2$ . The force variation

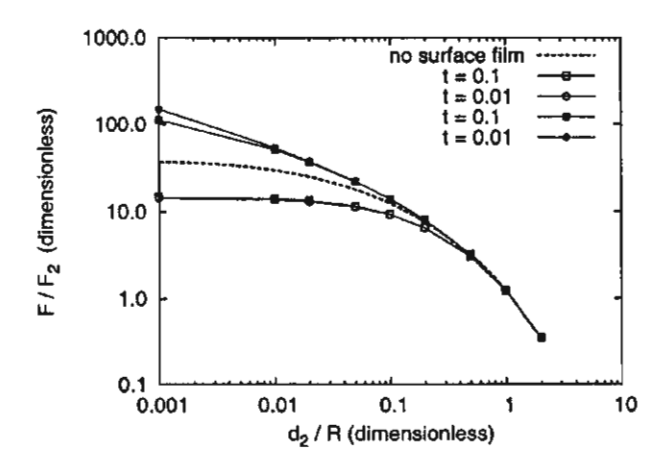
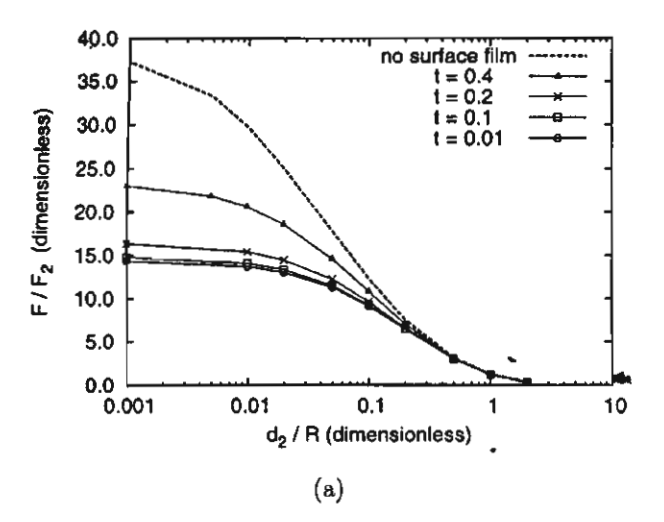


FIG. 13. Force in the arrangement of two particles under a uniform field. The symbols □ and ○ represent the conductor-core particles, whereas ■ and ● represent the dielectric-core particles.



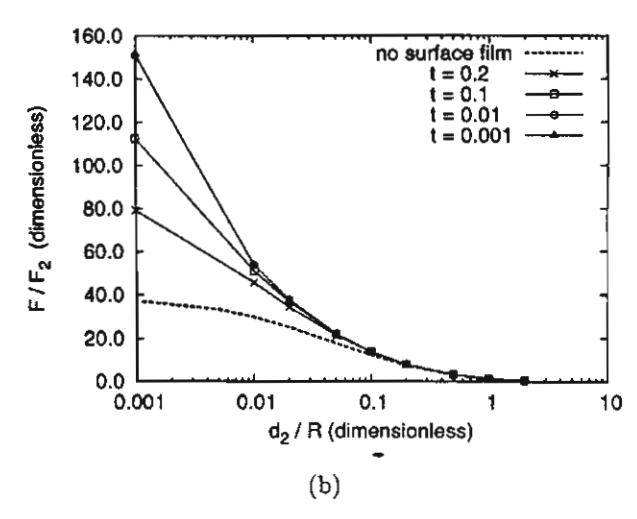


FIG. 14. Variation of force on each particle type with the film thickness. (a) Conductor core and (b) perfect-dielectric core.

with the film thickness can be more clearly observed in Fig. 14, where the force is separately presented for each particle type. The saturation of force as  $t/R \rightarrow 0$  and  $d_2/R \rightarrow 0$  can be seen in Fig. 14(a) but not in Fig. 14(b). This is because, for the condition of fixed  $\sigma_{II}$ , as t decreases,  $\sigma_F$  converges to zero for the conductor-core particle but converges to  $\infty$  for the dielectric-core particle. The increase of  $\sigma_F$  of the dielectric-core particle leads to the singular electric field and force if  $d_2=0$ . Therefore, we see the force in Fig. 14(b) at a very small t/R constantly becomes stronger with decreasing  $d_2$ .

## V. NUMERICAL RESULTS WHEN A SURFACE FILM IS REPRESENTED BY THE SURFACE CONDUCTIVITY

A surface film is often treated as a zero-thickness medium of the surface conductivity  $\sigma_S$  in the numerical field calculation methods. This section compares the calculation results by the method of images, the analytical method with those by a numerical method in which a surface film is replaced with a surface conductivity. The numerical method applied here is the boundary element method (BEM). The

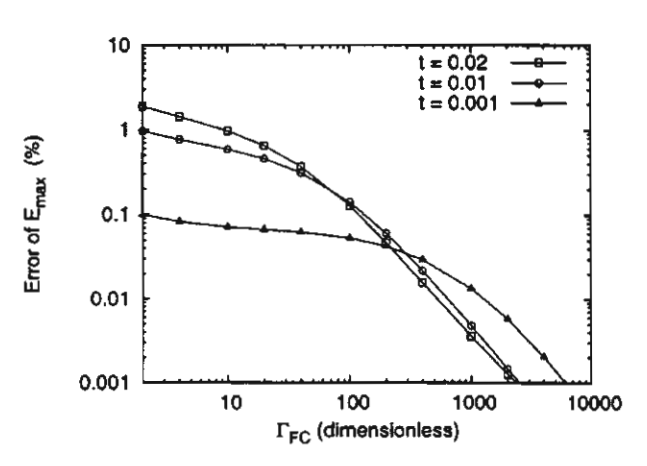


FIG. 15. Errors of the maximal electric field by the BEM on the particles remote from each other.

BEM is one of the boundary-subdivision methods, which generally give more accurate results of the electric field than the domain-subdivision ones. The treatment of the surface films in the BEM is referred to Refs. 16 and 17. We have carried out the calculations for the arrangement of Fig. 8, where  $\sigma_C = \sigma_E = 1$ . The film thickness t and conductivity  $\sigma_E$ have been varied to study their effects on the results. The BEM applies the axisymmetrical condition of the arrangement to realize the high accuracy as well as the symmetry with respect to the midplane between the particles to reduce the calculation time. We also use a fine subdivision on each particle surface (480 second-order elements from  $\theta$ =0° -180°) to reduce the errors in the surface modeling and the discretization of the variables involved. Accordingly, we shall consider that the errors of the results obtained from the BEM are predominated by the representation of a real surface film with a zero-thickness one.

Figure 15 presents the errors of the electric field calculated by the BEM, where the particles are remotely located. The electric field is evaluated at the maximal-field position  $p_2$  shown in Fig. 8. As can be seen from the figure, the errors decrease with increasing  $\Gamma_{FC}$ . The decrease becomes steeper with  $\Gamma_{FC}$  when the film conductivity becomes predominant. The steeper transition occurs at smaller  $\Gamma_{FC}$  for the particle having a thicker film. For small  $\Gamma_{FC}$ , the errors are higher on the particle having a thicker film. However, for the case where the external field is uniform, the errors are very low, less than 2%.

Figure 16 shows the errors of the field when the particles are closely spaced. The errors are evidently greater than those in Fig. 15. The figure shows that a thicker surface film results in higher errors for identical  $\Gamma_{FC}$ . The variation of the errors with  $\Gamma_{FC}$  is more complex where the particles are close to each other. With increasing  $\Gamma_{FC}$ , the errors of the electric field are magnified as the external field is composed of higher (j-1)th-order components but they are reduced by the predomination of the film conductivity, which makes the representation by  $\sigma_S$  more accurate. As a consequence, the errors in Fig. 16 may either increase or decrease with  $\Gamma_{FC}$ . Nonetheless, at a very high  $\Gamma_{FC}$ , the errors are reduced to

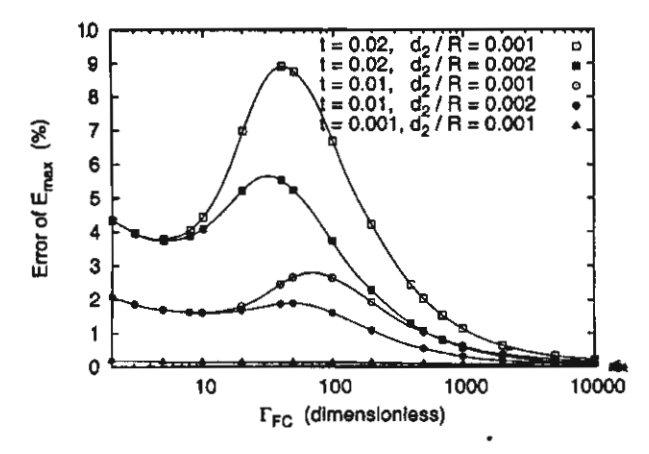


FIG. 16. Error of the maximal electric field by the BEM on the particles closely spaced.

lower than 1%. Furthermore, if the film is thin enough (e.g., t=0.001 in Fig. 16), the errors are very small even at low  $\Gamma_{FC}$ .

### VI. CONCLUSIONS

We have presented the analysis of the electric field and dielectrophoretic force on spherical particles with a surface film. The fundamental solutions, which can be utilized in the method of multipole images are presented for the various types of particles composed of a core and a surface film. We introduce the concept of the apparent conductivity  $\sigma_{Ii}$  to clarify the difference between the particle types. The analysis shows that the response of a particle with a surface film to an external field is unique and generally cannot be obtained by replacing the particle with a homogeneous particle. We have found that  $\sigma_{ij}$  varies with j differently between the conductor-core and the dielectric-core particles.  $\sigma_{Ii}$  is characterized by  $\sigma_F/t$  for the conductor-core particle but by  $\sigma_F t$ for the dielectric-core particle, where t and  $\sigma_F$  are the film thickness and conductivity. We have presented two numerical examples demonstrating the difference between the particles that exhibit an identical response to a uniform external field. The electric field and force are found smaller on the conductor-core particle but greater on the dielectric-core particle compared with the homogeneous particle without any surface film. We have shown that the propriety of treating a surface film as a zero-thickness medium of the surface conductivity depends not only on the film properties but also on the order of the external field.

### **ACKNOWLEDGMENT**

This work was financially supported by the Thailand Research Fund.

- <sup>1</sup>D. M. Taylor and P. E. Secker, *Industrial Electrostatics* (John Wiley, New York, 1994).
- <sup>2</sup>J. Robertson and B. R. Varlow, Proceedings of the 7th International Conference on Properties and Applications of Dielectric Materials (2003), p. 761.
- <sup>3</sup>T. C. Jordan and M. T. Shaw, IEEE Trans. Electr. Insul. 24, 849 (1989).
   <sup>4</sup>A. Inoune, U. Ryu, and S. Nishimura, Proceedings of the 8th International Conference of Electrorheological Fluids and Magnetorheological Suspensions, edited by G. Bossis (2001), pp. 23-29.
- <sup>5</sup>D. Adams and L. Johnston, Proceedings of the 8th International Conference on Electrorheological Fluids and Magnetorheological Suspensions, edited by G. Bossis (2001), p. 37.
- <sup>6</sup>P. Atten, C. Boissy, and J. N. Foulc, J. Electrost. 40-41, 3 (1997).
- <sup>7</sup>L. C. Davis, J. Appl. Phys. 73, 680 (1993).
- <sup>8</sup>C. W. Wu and H. Conrad, J. Appl. Phys. 81, 383 (1997).
- <sup>9</sup>C. W. Wu and H. Conrad, J. Appl. Phys. 81, 8057 (1997).
- <sup>10</sup>P. Gonon, J. N. Foulc, P. Atten, and C. Boissy, J. Appl. Phys. 86, 7160 (1999).
- <sup>11</sup>M. Washizu and T. B. Jones, IEEE Trans. Ind. Appl. 32, 233 (1996).
- <sup>12</sup>B. Techaumnat and T. Takuma, IEEE Trans. Dielectr. Electr. Insul. 10, 623 (2003).
- <sup>13</sup>B. Techaumnat, B. Eua-arporn, and T. Takuma, J. Appl. Phys. **95**, 1586 (2004).
- <sup>14</sup>B. Liu, S. A. Boggs, and M. T. Shaw, IEEE Trans. Dielectr. Electr. Insul. 8, 173 (2001).
- <sup>15</sup>L. C. Davis, Appl. Phys. Lett. 60, 319 (1992).
- <sup>16</sup>A. Nicolas, J. L. Rasolonjanahary, and L. Krahenbuhl, IEEE Trans. Magn. 28, 1473 (1992).
- <sup>17</sup>B. Techaumnat, S. Hamada, and T. Takuma, J. Electrost. **56**, 67 (2002).
- <sup>18</sup>X. Tang, C. Wu, and H. Conrad, J. Appl. Phys. **78**, 4183 (1995).
- <sup>19</sup>A. Sihvola and I. V. Lindell, Proceedings of the Antenna and Propagation Society International Symposium (1988), p. 388.
- <sup>20</sup>A. H. Sihvola and J. A. Kong, IEEE Trans. Geosci. Remote Sens. GE-26, 420 (1988).
- <sup>21</sup>T. B. Jones, *Electromechanics of Particles* (Cambridge University Press, New York, 1995).
- <sup>22</sup>D. J. Griffiths, Introduction to Electrodynamics (Prentice-Hall Inc., New Jersey, 1989).

# Electric field and dielectrophoretic force on a dielectric particle chain in a parallel-plate electrode system

## B Techaumnat<sup>1</sup>, B Eua-arporn<sup>1</sup> and T Takuma<sup>2</sup>

- <sup>1</sup> Department of Electrical Engineering, Chulalongkorn University, Bangkok 10330, Thailand
- <sup>2</sup> Central Research Institute of Electric Power Industry, Tokyo 201-8511, Japan

E-mail: boonchai.t@chula.ac.th

Received 16 July 2004, in final form 8 October 2004 Published 19 November 2004 Online at stacks.iop.org/JPhysD/37/3337 doi:10.1088/0022-3727/37/23/017

#### Abstract

This paper presents results of calculations of the electric field and dielectrophoretic force on a dielectric particle chain suspended in a host liquid lying between parallel-plate electrodes. The method of calculation is based on the method of multipole images using the multipole re-expansion technique. We have investigated the effect of the particle permittivity, the tilt angle (between the chain and the applied field) and the chain arrangement on the electric field and force. The results show that the electric field intensification rises in accordance with the increase in the ratio of the particle-to-liquid permittivity,  $\Gamma_{\varepsilon}$ . The electric field at the contact point between the particles decreases with increasing tilt angle, while the maximal field at the contact point between the particles and the plate electrodes is almost unchanged. The maximal field can be approximated by a simple formula, which is a quadratic function of  $\Gamma_{\varepsilon}$ . The dielectrophoretic force depends significantly on the distance from other particles or an electrode. However, for the tilt angles in this paper, the horizontal force on the upper particle of the chain always has the direction opposite to the shear direction. The maximal horizontal force of a chain varies proportional to  $(\Gamma_{\varepsilon} - 1)^{1.7}$  if the particles in the chain are still in contact with each other. The approximated force, based on the force on an isolated chain, has been compared with our calculation results. The comparison shows that no approximation model agrees well with our results throughout the range of permittivity ratios.

## 1. Introduction

There are many applications of dielectric materials in the form of particles. For example, an electrorheological (ER) fluid is a suspension of dielectric particles in a host liquid [1]. The fluid exhibits a fast, reversible change in apparent viscosity under an electric field. The fluid has been proposed for a variety of applications such as hydraulic valves, clutches and shock absorbers. In many applications, ER fluids exist in small, uniform gaps between electrodes, which may be either coaxial cylinders or circular discs [2–4]. The configuration of parallel circular discs is also found in rheometers of the rotating-plate type. These arrangements are often simplified to arrangements

of parallel-plate electrodes in analysis, as the gap length is usually much smaller than the electrode dimensions.

The change in apparent viscosity of the ER fluid results from the interaction between suspended particles and the electric field. When an electric field, usually of the order of kilovolts per millimetre, is applied to the fluid, the field aligns the particles into chains parallel to its direction. As the chains increase the flow resistance, the apparent viscosity is closely related to the dielectrophoretic force acting on the chains. Up to now, there have been several reports that have analysed the shear yield stress of ER fluids. Many of them have determined the shear yield stress based on the force on an isolated particle-chain. Davis calculated the electric field on

a two-particle chain using an integral equation method [5]. The force on the particles was approximated from the gap field by integrating Maxwell's stress. Another analysis on a two-particle chain by Gonon et al [6] was performed using an equivalent electrical circuit. The circuit was based on the conduction model for particles composed of a conducting core and a weakly conductive film. The force was calculated over the mid-plane between the particles. Alternatively, Wu and Conrad [7,8] reported on analysis of the force on a chain with an infinite number of particles. The particles under consideration consisted of an insulating core and a conductive surface film. The electric field was calculated using the conduction model. All the analysis considered the cases in which the chain was parallel to the applied field. An approximation was made that the electric field direction in the gap between particles principally coincided with the direction of the applied field [6-8]. The force on a chain making a non-zero angle with the applied field was assumed to be induced only by the electric field parallel to the chain. Besides, the presence of the electrodes was neglected in the analysis.

This paper presents the results of calculation of the electric field and dielectrophoretic force on a particle chain between two parallel-plate electrodes. Using the method of multipole images [9], we can calculate the electric field without any approximation regarding the field distribution. The calculation has been carried out for three-dimensional arrangements in which the particle chain is not parallel to the applied field. We have partly reported the results of calculation for particles between parallel-plate electrodes [9]. The results have shown that the effect of the electrode is small if a particle chain is separated from an electrode roughly by the particle radius or greater. However, when the gaps between the chain and electrodes are smaller than those in [9], the existence of the two electrodes is not negligible, which plays a significant role in the change in apparent viscosity of the fluid. This paper considers the deformation (tilting and separation) of a particle chain bridging two parallel-plate electrodes, and reports a detailed analysis of the effect of the distance from the electrodes. We also vary the particle permittivity and the geometrical arrangement of the chain under a shear stress to make clear the behaviour of the force.

### 2. Dielectrophoretic force

The dielectrophoretic force is described as the force induced by a spatially non-uniform electric field on a polarized but uncharged particle. The force exists only if the particle polarizability differs from that of the surrounding medium, i.e. their permittivities are different. If the particle permittivity is greater than the surrounding one, then 'positive dielectrophoresis' occurs. The induced force pulls the particle towards the region of higher electric field. In contrast, 'negative dielectrophoresis' occurs if the particle permittivity is less than the surrounding one. The force repels the particle towards the region of lower field.

On a particle located under an electric field E, sufficiently far from other particles and electrodes, the dielectrophoretic force, F, can be approximated by the point-dipole model [10].

$$F = 2\pi \varepsilon_{\rm E} R_{\rm p}^3 \beta \nabla E^2, \tag{1}$$

where  $\varepsilon_E$  is the surrounding permittivity,  $R_P$  the particle radius and  $\beta$  the Clausius-Mossotti factor, defined for a particle permittivity,  $\varepsilon_P$ , as

$$\beta = \frac{\varepsilon_{\rm P} - \varepsilon_{\rm E}}{\varepsilon_{\rm P} + 2\varepsilon_{\rm E}}.\tag{2}$$

It can be seen easily from equation (2) that  $F \neq 0$  only if  $\beta \neq 0$  and  $\nabla E^2 \neq 0$ .

However, the behaviour of the force is more complicated for particles very close to each other. The point-dipole approximation becomes inadequate, and we must consider higher-order multipoles. Figure 1 shows the distributions of the electric field and force on a two-particle chain under a uniform field for positive dielectrophoresis ( $\beta=1.5$ ). In figure 1(a), we can clearly see electric field intensification near the contact point between the particles. The downward force due to the high field near the contact point is predominant over the force on the rest of particle surface, resulting in a net force attracting the particles together. The electric field and force change as in figure 1(b) (left), where the chain is tilted by 15° while the particles are still in contact. The direction of the force is obviously influenced by the change in chain direction. If the particles are separated by a small gap as in figure 1(c), the

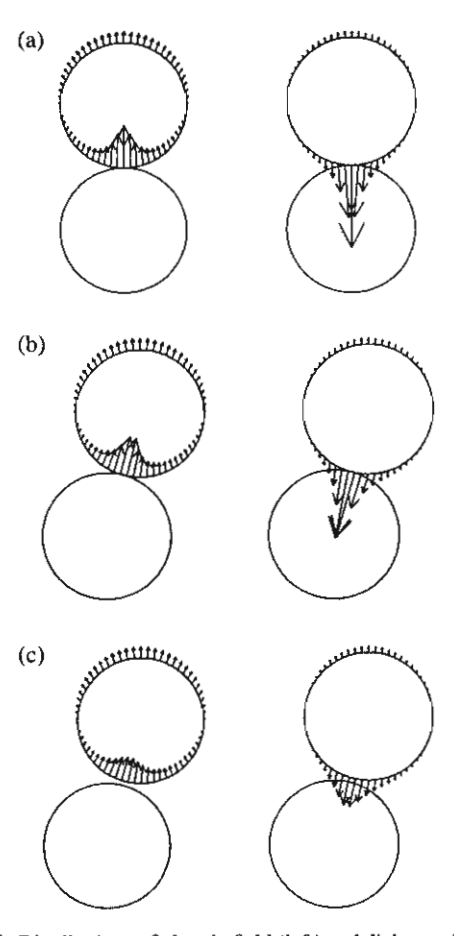


Figure 1. Distributions of electric field (left) and dielectrophoretic force (right) on the upper particle of a two-particle chain under a uniform field. (a) A chain aligned parallel to the electric field. (b) A chain tilted to make an angle of 15° with the electric field. (c) A tilted chain in which particles are separated by a small distance  $(\approx 0.07 R_P)$ .

field and force resemble those in figure 1(b) but are of smaller magnitudes.

For cases where the particles or the surrounding medium is not a perfect dielectric, dielectrophoresis is characterized by the complex Clausius-Mossotti factor  $\beta'$  including the conductivity,  $\sigma$ , and the angular frequency,  $\omega$ ,

$$\beta' = \frac{\varepsilon_{\rm p}' - \varepsilon_{\rm E}'}{\varepsilon_{\rm p}' + 2\varepsilon_{\rm E}'},\tag{3}$$

where the complex permittivity  $\varepsilon' = \varepsilon - i\sigma/\omega$ .

## 3. Arrangements

The arrangements for the calculation are two dielectric particles in a host dielectric liquid which lies between two parallel-plate electrodes. When the electrodes are energized to have a potential difference  $\phi_0$ , an external electric field in the vertical direction induces a dielectrophoretic force on the particles. If the force is sufficiently strong, it will align the particles to form a particle chain across the electrodes in the field direction as shown in figure 2. In practical ER fluids, the particle chains are composed of a large number of particles. The largest effect on the electric field and resultant force is made by the interaction with the adjacent particle, or an electrode in the case of a particle at the chain edge. The behaviour of the field at the end of the two-particle approximation corresponds mainly to that of a particle at a chain edge, while the behaviour near the middle corresponds to that of an intermediate particle. In this work, we are interested in the situation where a chain starts tilting to be non-parallel with the applied field. The chain is still close to the electrodes, and both electrodes are included in the calculation model. In the calculation, the particle radius, R, is normalized to a unit value. The electrode separation, D, is chosen so that there is no space between the particle chain and the electrodes in figure 2 (D = 4R). Figure 3(a) shows the electric field and force on the particle chain before application of shear. The parallel plates lead to the symmetry of electric field between the upper and lower halves of the particle in figure 3(a). Consequently, the forces on the upper and lower halves completely cancel each other; thus, the net force on the particle is zero.

Under application of shear, the upper plate slides in the horizontal direction, and the particle chain is tilted from a vertical position. As a result, the electric field and force change from those in figure 3(a). Figures 3(b) and (c) display the distributions of the electric field and force on the tilted chain without and with a gap between the particles, respectively. With the existence of the plate electrodes, the field and force

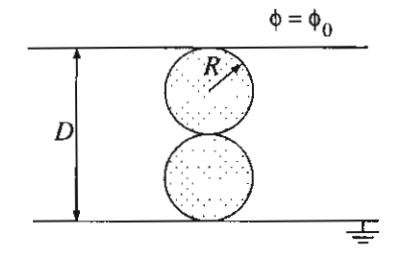


Figure 2. A particle chain formed by the dielectrophoretic force.

in figures 3(b) and (c) are significantly different from those in figures 1(b) and (c). However, the field and force between the particles in figure 3 are still very similar to those in figure 1 as the interaction between particles is predominant in the region. In this paper, we consider four geometrical arrangements of the chain for any tilt angle,  $\alpha$ , between the chain and the applied field, as shown in figure 4. The four arrangements are as follows:

- (i) In figure 4(a), the chain is split by a distance  $d = 2R[(\cos \alpha)^{-1} 1]$  so as to remain in contact with both electrodes.
- (ii) In figure 4(b), the chain rotates, and the particles are still in contact with each other but no more in contact with the electrodes.
- (iii) In figure 4(c), the chain is split, and the particles are in contact neither with each other nor with the electrodes. This is considered to be a transition arrangement between the first two arrangements. The separation between the particles is taken as half of that in figure 4(a) in the calculation.
- (iv) In figure 4(d), the chain rotates, while it remains in contact with the lower electrode.

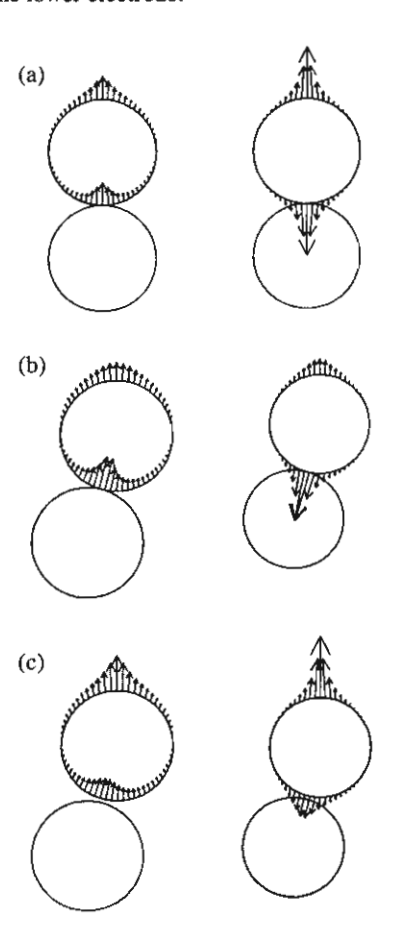


Figure 3. Distributions of electric field (left) and dielectrophoretic force (right) on the upper particle of a two-particle chain between two parallel-plate electrodes. (a) A chain aligned parallel to the applied electric field. (b) A chain tilted to make an angle of 15° with the field while the lower particle remains on the electrode. (c) A tilted chain in which particles are in contact with their closest electrodes and separated by the same distance as in figure 1(c).

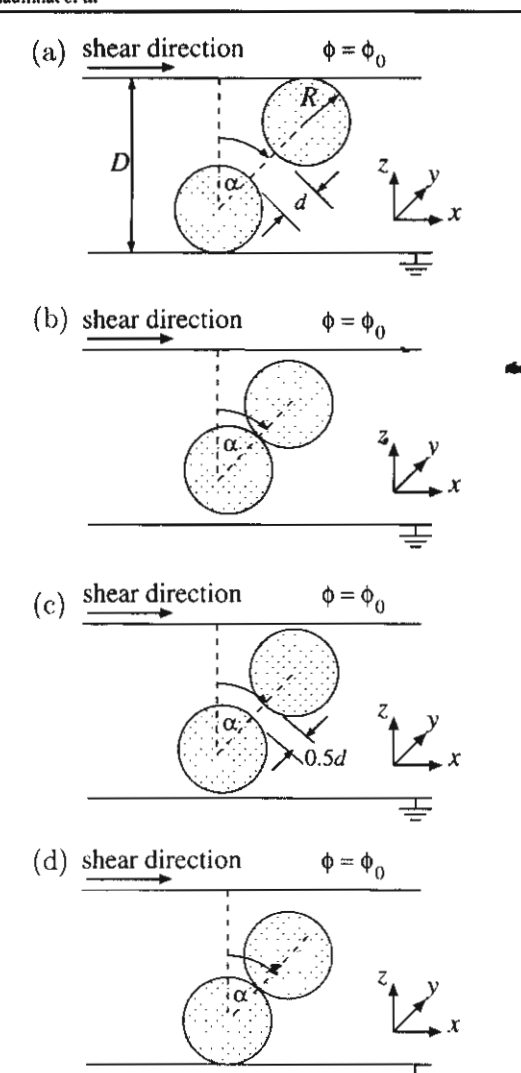


Figure 4. Assumed deformation of a particle chain during shear.

For all the arrangements, we assume that the particles and the host liquid are perfect dielectrics (i.e. they possess no conductivity) and their permittivities are independent of the electric field. The permittivities of the particles and host liquid are denoted by  $\varepsilon_P$  and  $\varepsilon_L$ , respectively. We have calculated the electric field and force for  $0^{\circ} \leqslant \alpha \leqslant 45^{\circ}$  and  $\varepsilon_P/\varepsilon_L = 4$ , 8 and 12. For cases of ac fields, if the conductivity is a constant independent of the electric field, the material conductivity can be readily taken into consideration by replacing  $\varepsilon$  with the complex permittivity as mentioned in the previous section.

## 4. Analytical method

The method of calculation is based on the method of images [11]. However, in addition to using point charges, we use multipoles to obtain the solution. For each particle, the potential is expressed with a set of spherical-harmonics functions expanded around its centre. The potentials,  $\phi_I$  in the interior and  $\phi_E$  in the exterior, of a particle are written

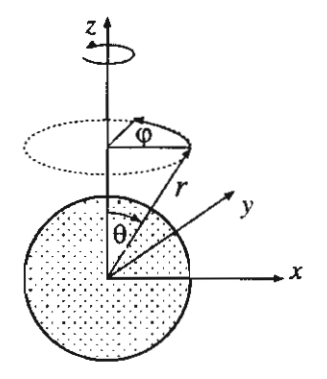


Figure 5. Spherical coordinates for expressing the potential about the particle centre.

as follows:

$$\phi_{\bar{l}} = \sum_{j=0}^{\infty} \sum_{k=-j}^{j} L_{j,k} r^{j} \bar{P}_{j,\{k\}}(\cos \theta) \exp(ik\varphi), \qquad (4)$$

$$\phi_{E} = \sum_{i=0}^{\infty} \sum_{k=-i}^{j} \left( M_{j,k} r^{j} + \frac{B_{j,k}}{r^{j+1}} \right) \tilde{P}_{j,|k|}(\cos \theta) \exp(ik\varphi), \quad (5)$$

where  $L_{j,k}$ ,  $M_{j,k}$  and  $B_{j,k}$  are the coefficients to be determined,  $(r, \theta, \varphi)$  are the spherical coordinates in which the particle centre is taken as the origin (see figure 5) and  $\tilde{P}_{j,|k|}$  is the normalized associated Legendre function.  $\tilde{P}_{j,|k|}$  is related to the associated Legendre function,  $P_{j,|k|}$ , by

$$\bar{P}_{j,|k|}(x) = \sqrt{\frac{(n-|m|)!}{(n+|m|)!}} P_{j,|k|}(x)$$
 (6)

for  $-1 \le x \le 1$ . Note that the former and the latter terms on the right-hand side of equation (5) represent the potentials due to charges located in the interior and exterior of the particle, respectively.

In the calculation, we compute repetitively the coefficients  $L_{j,k}$ ,  $M_{j,k}$  and  $B_{j,k}$  until all the boundary conditions on the particle and electrode surfaces are satisfied. The repetition procedure, using the multipole re-expansion and the appropriate multipole images for the arrangements of particles and electrodes, is described in [9,12]. However, the presence of more than one electrode complicates the calculation procedure. We explain the calculation procedure for a multipole and two parallel-plate electrodes in the appendix.

The analytical method has the main limitation that it is applicable only for certain configurations where we know the solutions of images. However, where applicable, the analytical method usually gives results of better accuracy, and often takes a shorter calculation time than numerical field calculation methods. This is because errors in boundary simulation are involved in the numerical methods, especially in the simulation of three-dimensional curved surfaces. Furthermore, for arrangements having triple-junction points, the points where three media (conductor or dielectric) meet each other, electric field enhancement often occurs near the points. Thus, the numerical methods need very fine subdivision of domains or boundaries for attaining a high accuracy. In our calculation arrangements, the contact point

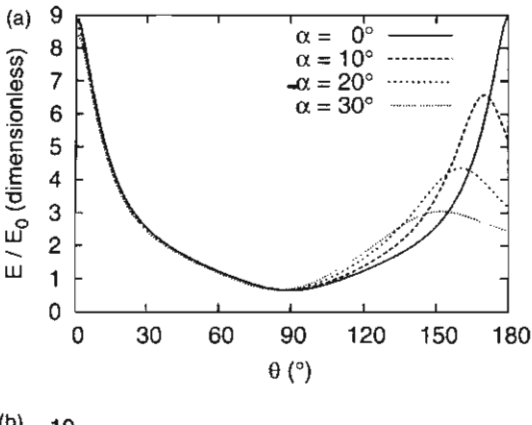
between the particles and the contact point between the particle and the plate electrode are triple-junction points. We have already reported a comparison between the analytical method and the boundary element method, a numerical field calculation method, for axisymmetrical arrangements [12]. For the arrangements including the two plate electrodes, we have confirmed that the electric field cannot be computed easily with a higher accuracy using the numerical methods than using the analytical one.

After we obtain the potential coefficients for each particle, we compute the dielectrophoretic force on the particle by integrating Maxwell's stress on the particle surface.

### 5. Results and discussion

#### 5.1. Electric field distribution on particle surface

Figure 6 shows the electric field distributions along the  $\theta=0^\circ$  to  $180^\circ$ ,  $\varphi=180^\circ$  line on the upper particle in the arrangement of figure 4(a) for the permittivity ratio  $\Gamma_\varepsilon=\varepsilon_P/\varepsilon_L=4$  and  $\alpha=0^\circ$ ,  $10^\circ$ ,  $20^\circ$  and  $30^\circ$ . The electric field is normalized by  $E_0=\phi_0/D$ , the applied field in the absence of particles. For this arrangement, the field is maximal at  $\theta=0^\circ$ , the contact point between the particle and the upper electrode. There is also a local maximal field at  $\theta=180^\circ-\alpha$ , which is the point closest to the lower particle. The maximal electric field does not vary much with  $\alpha$ , whereas the local maximal field decreases considerably with increasing  $\alpha$ . It can also



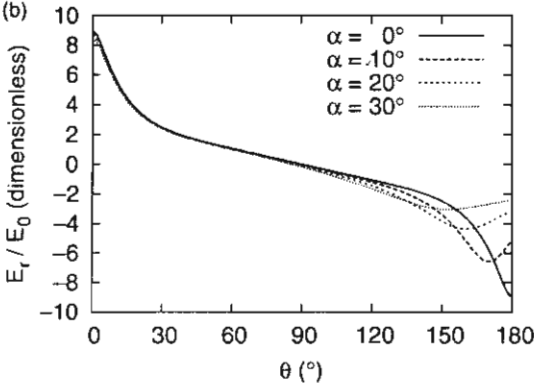


Figure 6. Electric field distributions on the upper particle in figure 4(a) for  $\Gamma_{\kappa} = 4$ : (a) total electric field; (b) normal component of electric field.

be inferred from the figure that, in the high-field regions, the normal component of the electric field is predominant over the tangential one. For a higher mismatch between  $\varepsilon_P$  and  $\varepsilon_L$  (higher  $\Gamma_\varepsilon$ ), we have found that the field distributions remain similar, but the field is more intensified in the high-field regions.

For  $\alpha = 0^{\circ}$ , the contact-point electric fields at  $\theta = 0^{\circ}$  and 180° are identical since the arrangement reduces to an infinite number of particles aligned parallel to the applied field. The contact-point electric field,  $E_c$ , may be approximated as a function of the permittivity ratio by the following equation [13]:

$$E_{\rm c} = \frac{\Gamma_{\rm e}(\Gamma_{\rm e} + 1)}{2} E_0. \tag{7}$$

Figure 7 compares the approximation by (7) and the calculation results. The figure shows a good agreement between the approximation and the results of calculation for  $\Gamma_{\varepsilon} = 1-64$ .

Figure 8 presents the distributions of the total field on the upper particle in the arrangement of figure 4(b). (Note that for  $\alpha=0^{\circ}$ , the electric field is the same in all the arrangements of figure 4.) The electric field is maximal at  $\theta=180^{\circ}-\alpha$ , which is the contact point between the particles. The field is locally maximal at  $\theta=0^{\circ}$ , the point closest to the upper electrode. The variation of the maximal field is different from that in figure 6 as it depends greatly on  $\alpha$ .

The arrangement in figure 4(c) may exist during the transition between the chains in figures 4(a) and (b). Figure 9

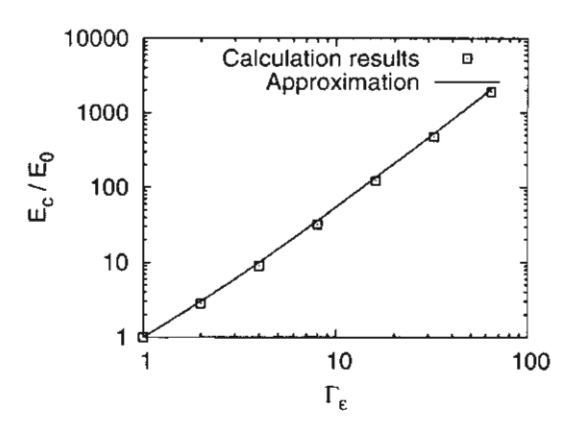


Figure 7. Electric field at the contact points for  $\alpha = 0$ .

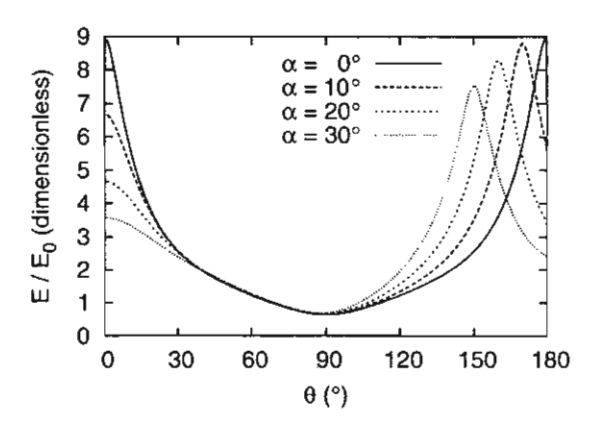


Figure 8. Electric field distributions on the upper particle in figure 4(b) for  $\Gamma_{\varepsilon} = 4$ .

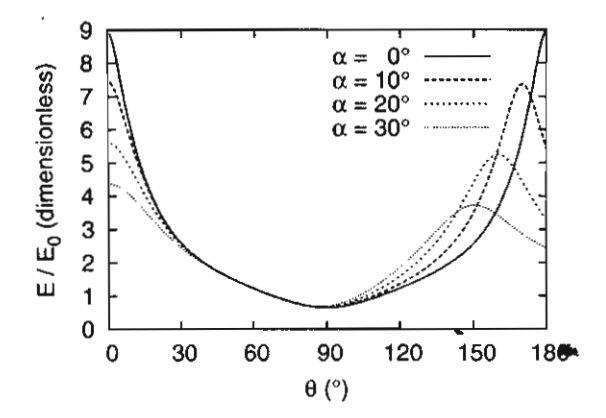


Figure 9. Electric field distributions on the upper particle in figure 4(c) for  $\Gamma_{\epsilon} = 4$ .

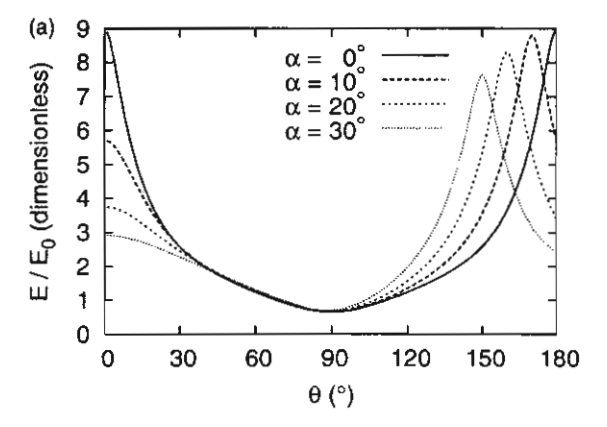
presents the field distributions on the upper particle for comparison. The figure shows that both electric fields at  $\theta=0^\circ$  (closest to electrode) and  $\theta=180^\circ-\alpha$  (closest to the lower particle) decrease considerably when  $\alpha$  increases. The maximal field is located at  $\theta=0^\circ$ . However, the maximal-field position possibly depends on the distance between the particles and the separations between them and the electrodes.

While symmetry with the middle plane between the electrodes exists in the arrangements of figures 4(a)–(c), the fields on the upper and lower particles in the arrangement of figure 4(d) are not identical. The fields are presented in figure 10. Figure 10 shows the electric field distributions along the  $\varphi=180^\circ$  line on the upper particle and the  $\varphi=0^\circ$  line on the lower particle for  $\Gamma_\varepsilon=4$ . The field distribution in figure 10(a) is similar to that in figure 8, but lower than that in figure 8 near  $\theta=0^\circ$ . For the lower particle, the field at  $\theta=180^\circ$  does not vary greatly with  $\alpha$  since the particle remains in contact with the lower electrode. The field strength is more or less the same as that of the field at  $\theta=0^\circ$  in figure 6(a).

## 5.2. Dielectrophoretic force on the particle chain

We consider the horizontal force,  $F_x$ , and vertical force,  $F_z$ , on the particles. There is no net force in the y-direction because of the symmetry of the arrangement. The spatial deformation of the chain from figure 2 results in a non-zero net force on each particle. As already shown in figure 3(c), where  $\alpha=15^\circ$ , the electric field becomes non-symmetrical after the deformation. It can be seen from the figure that the net horizontal force is mainly induced by the interaction between the particles.

Figure 11 shows the variation of  $F_x$  and  $F_z$  with  $\alpha$  on the upper particle in the arrangement of figure 4(a). The forces are normalized by  $F_0 = \frac{1}{2} \varepsilon_L E_0^2 R^2$ , the force acting on any  $R \times R$  square element of the electrodes in the absence of particles. The directions of  $F_x$  and  $F_z$  conform with the axes in figure 4. Figure 11 shows that, for the range  $0 < \alpha \le 45^\circ$ ,  $F_x$  resists the shear applied to the upper electrode since  $F_x < 0$  and  $F_z$  attracts the particle to the upper electrode. The angles  $\alpha_{\max F_z}$  and  $\alpha_{\max F_z}$  at which  $F_x$  and  $F_z$ , respectively, become maximal depend on  $\Gamma_\varepsilon$ . Both  $\alpha_{\max F_z}$  and  $\alpha_{\max F_z}$  tend to be smaller for higher  $\Gamma_\varepsilon$ . The maximal  $F_x$  and  $F_z$  increase with increasing  $\Gamma_\varepsilon$ , but not linearly.



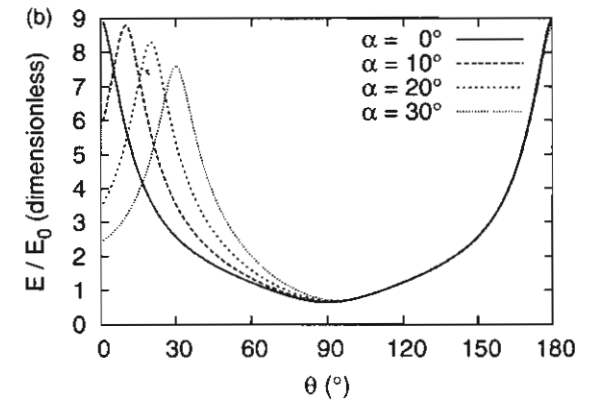


Figure 10. Electric field distributions on the particles for  $\Gamma_{\epsilon}=4$ : (a) the upper particle; (b) the lower particle.

Figure 12 shows  $F_x$  and  $F_z$  on the upper particle in the arrangement of figure 4(b). In this arrangement, the particles have moved adrift from the electrodes, but are still in contact with each other. The electric field on the particle surface near the electrode decreases with increasing  $\alpha$  to a greater extent than does the field near the contact point (see figure 8). This is because the particle becomes farther from the upper electrode when  $\alpha$  increases. The electric field in the former region contributes mainly to an upward  $F_z$  attracting the particle to the upper electrode, whereas that in the latter region attracts the particles together, resulting in the leftward  $F_x$  and downward  $F_{\tau}$ . For this arrangement, the force between the particles is predominant over the one between the particle and electrode; thus,  $F_z$  is negative for most values of  $\alpha$ . However,  $F_z$  is slightly weaker for this arrangement than that in figure 11(b). By contrast,  $F_x$  is much stronger in figure 12(a).

Figure 13 shows the forces for the arrangement of figure 4(c).  $F_x$  in figure 13(a) varies with  $\alpha$  as in figure 11(a), but  $F_x$  is stronger for this arrangement.  $F_z$  in figure 13(b) has an upward direction, attracting the particle to the upper electrode. The magnitude of  $F_z$  is much smaller than in figures 11 and 12. With increasing  $\alpha$  in this arrangement, the force attracting the particle to the upper electrode decreases as the separation from the electrode increases. In contrast, the force due to the interaction between particles is lowered by two factors. The first is the widened separation between the particles. The second is the reduction of the field component parallel to the chain. Figure 13(b) implies that the arrangement

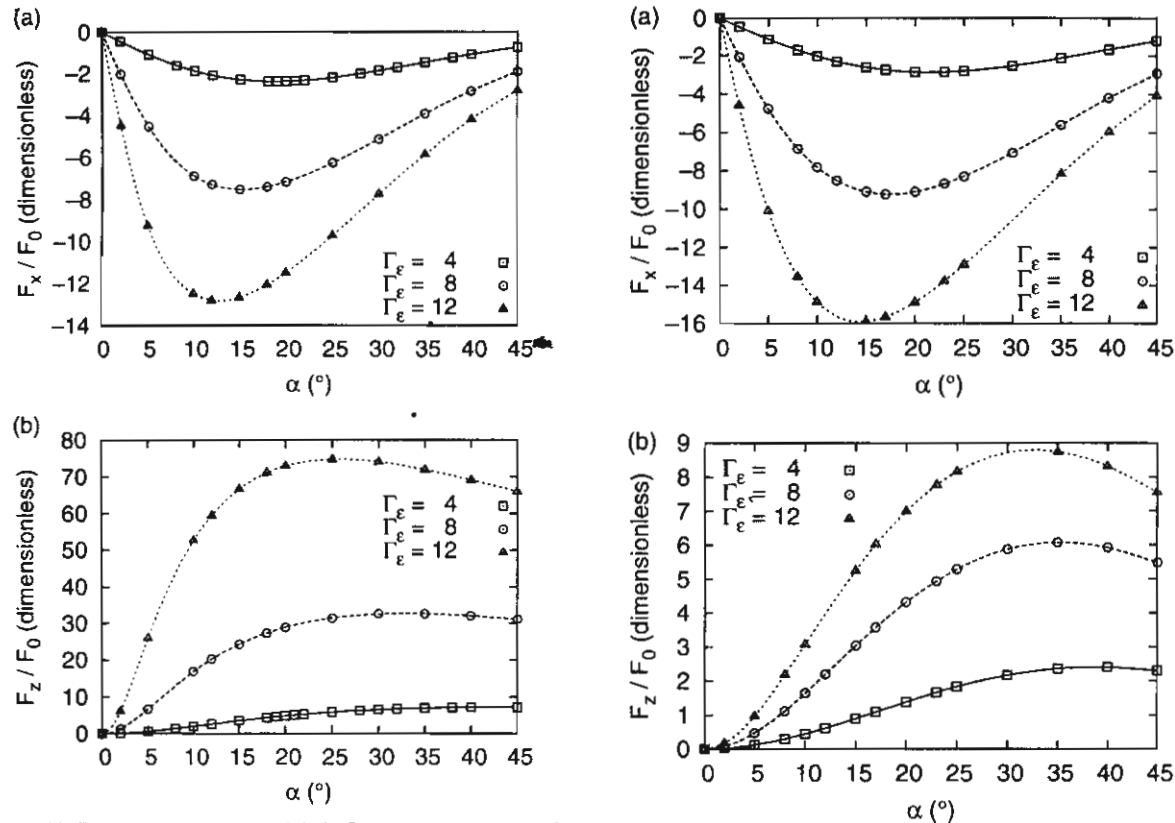


Figure 11. Forces on the upper particle in figure 4(a): (a)  $F_x$ ; (b)  $F_z$ .

(a) 0

-5

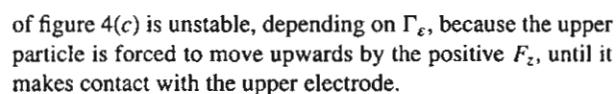


Figure 13. Forces on the upper particle in figure 4(c): (a)  $F_x$ ; (b)  $F_z$ .

-10makes contact with the upper electrode. For the arrangement of figure 4(d), the forces on the upper -15 and lower particles are different. Figures 14 and 15 present -20 the forces on the upper and lower particles, respectively. In -25 figure 14, the force variation for the upper particle is similar -30 to that in figure 12 for the arrangement of figure 4(b), but both -35  $F_x$  and  $F_z$  are slightly stronger. Among all the arrangements, this one possesses the highest values of the maximal  $F_x$  and -40 20  $F_z$ .  $F_x$  acting on the lower particle is similar to that on the 0 10 15 25 30 35 40 upper particle (but has the opposite sign), while  $F_z$  differs α (°) considerably from that on the upper particle. For the lower particle,  $F_z$  has a downward direction. Lastly, it is to be noted 0 that, for all the arrangements we consider here,  $F_x$  on the upper -10particles has a direction opposite to the shear direction. -20

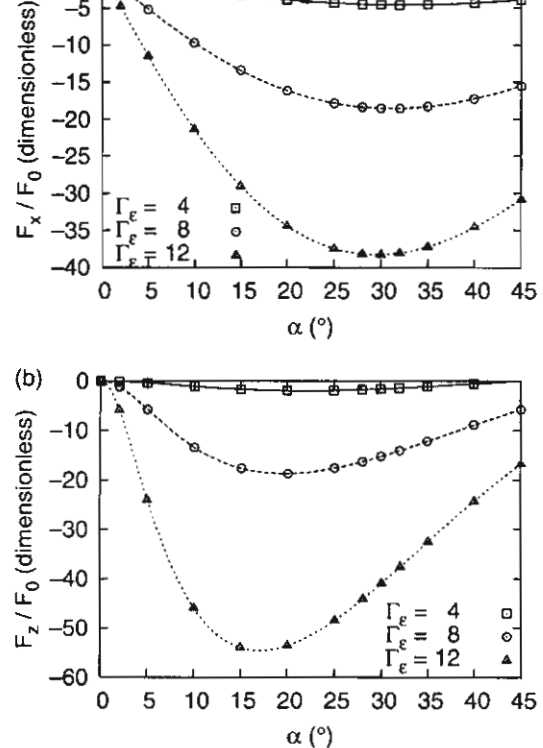
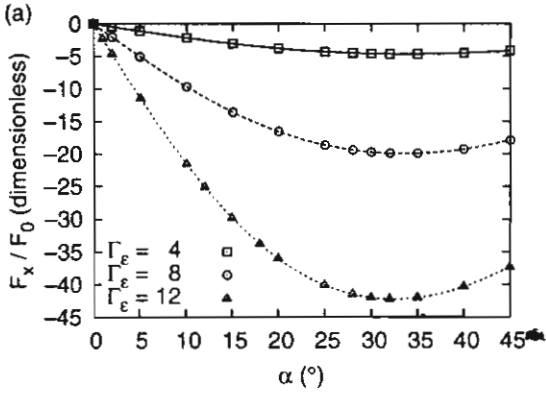


Figure 12. Forces on the upper particle in figure 4(b): (a)  $F_x$ ; (b)  $F_z$ .

### 5.3. Discussion of the dielectrophoretic force

The maximal horizontal force,  $\max\{F_x\}$ , on an isolated particle-chain was used to determine the shear yield stress of ER fluids in many reports. Mostly,  $max\{F_x\}$  was calculated based on the force,  $F_{\alpha 0}$ , acting on the chain when it is aligned parallel to the applied field,  $E_0$  (i.e.  $\alpha = 0$ ). However, there were different approaches to evaluating  $F_{\alpha 0}$ . It could be obtained for a two-particle chain [5,6] or for a chain having an infinite number of particles [7,8]. For the latter case where the net force on any particle was zero,  $F_{\alpha 0}$  was taken as the



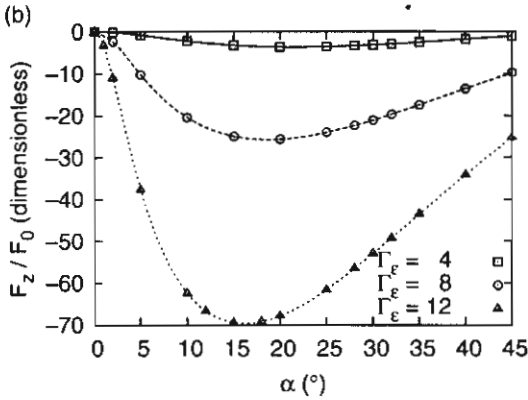
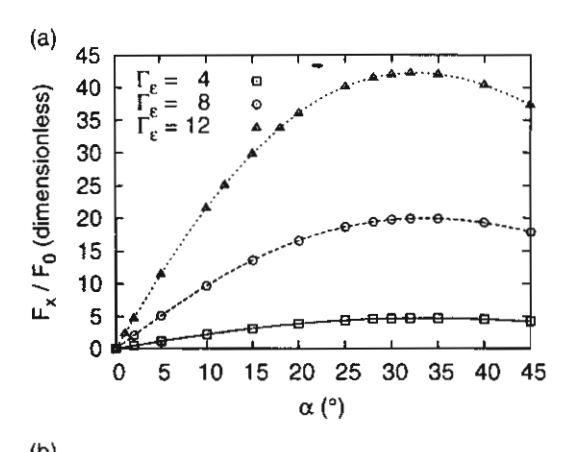


Figure 14. Forces on the upper particle in figure 4(d): (a)  $F_x$ , (b)  $F_z$ .



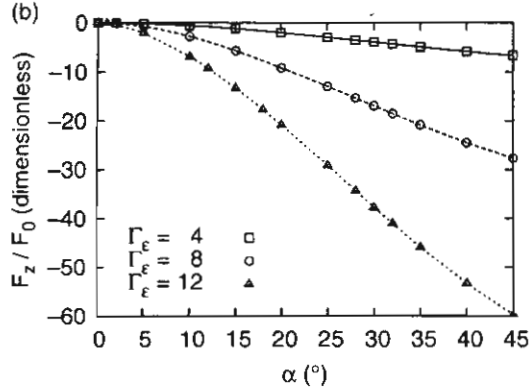


Figure 15. Forces on the lower particle in figure 4(d): (a)  $F_x$ , (b)  $F_z$ .

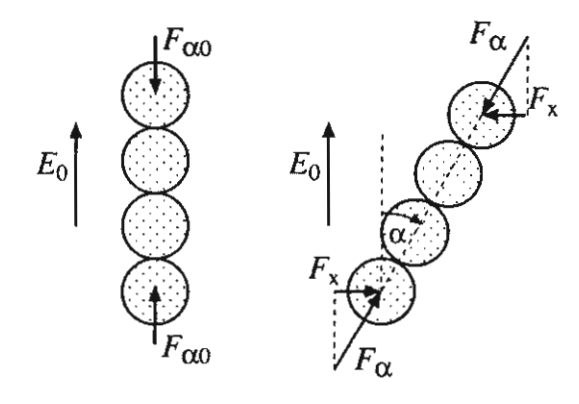


Figure 16. An isolated chain under an external field.

sum of the forces on the upper or lower half of any particle in the chain.

When the particle chain is bent to make an angle  $\alpha$  with the applied field,  $E_0$ , as shown in figure 16, the following assumptions were often made:

- Only E<sub>0</sub> cos α, the component parallel to the chain, contributes to the force. (E<sub>0</sub> sin α, the component perpendicular to the chain, is neglected.)
- · The effect of electrodes is neglected.

Under the above assumptions, we obtain the following relation for the electric field, E, and its normal component,  $E_n$ , at any point on the particle surface.

$$\frac{E_{\alpha}}{E_{\alpha 0}} = \frac{E_{n,\alpha}}{E_{n,\alpha 0}} = \cos \alpha, \tag{8}$$

where the subscripts  $\alpha 0$  and  $\alpha$  denote the values for  $\alpha = 0$  and any  $\alpha$ , respectively.  $F_{\alpha}$  in figure 16 can be written as an integral of Maxwell's stress over the particle surface,

$$F_{\alpha} = \int \left( \varepsilon_{\rm L} E_{\alpha} E_{\rm n,\alpha 0} - \frac{1}{2} \varepsilon_{\rm L} E_{\alpha}^2 n \right) \, \mathrm{d}s, \tag{9}$$

where n is the unit normal vector on the particle surface. From equations (8) and (9), it can be inferred that  $F_{\alpha} = F_{\alpha 0} \cos^2 \alpha$ . The horizontal force for the tilt angle,  $\alpha$ , in figure 16 approximates to [6]

$$F_x(\alpha) = F_{\alpha 0} \cos^2 \alpha \sin \alpha. \tag{10}$$

Then,  $\max\{F_x\}$  is defined as

$$\max\{F_x\} = \max\{F_{\alpha 0} \cos^2 \alpha \sin \alpha\} = F_{\alpha 0} \times \max\{\cos^2 \alpha \sin \alpha\}.$$
 (11)

From equation (11), the angle  $\alpha_{\max F_i}$ , at which the maximal  $F_x$  occurs, is about 35.3°, independent of  $\Gamma_{\varepsilon}$ , and

$$\max\{F_x\} \approx 0.385 F_{\alpha 0}.\tag{12}$$

In comparison, our calculation results show that if a particle chain deforms as in figure 4(a) or (c),  $\alpha_{\max F_x}$  is much lower than 35.3° and dependent on  $\Gamma_{\varepsilon}$ . For the chain arrangements in figures 4(b) and (d),  $\alpha_{\max F_x}$  varies slightly between 30° and 35°, which is close to the approximation. For reference, figure 17 gives  $F_x$  on the two-particle chain making different angles with an applied uniform field (without the plate electrodes). The angle  $\alpha_{\max F_x}$  in figure 17 agrees well with the approximation; thus,  $\alpha_{\max F_x}$  is not affected

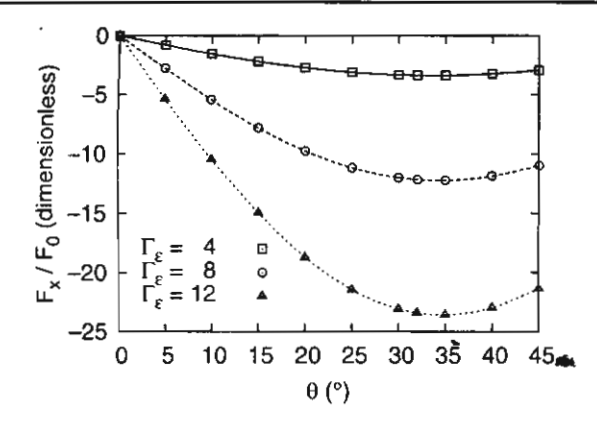


Figure 17. Horizontal force on the upper particle of a two-particle chain without the presence of the plate electrodes.

**Table 1.**  $\max\{F_x\}/F_0$  for isolated chains of different particle numbers.

Particle	$\Gamma_{\varepsilon}$		
number	4	8	12
2	2.45	9.96	20.4
32	3.05	14.0	31.3
$\infty$	9.24	28.3	57.9

significantly by the electric field perpendicular to the chain. Comparing figure 17 with figures 12(a) and 14(a), we can see the effect of an electrode separated from a particle chain by a small distance. While the presence of the electrode affects  $\alpha_{\max F_i}$  slightly, it increases the magnitude of the force considerably.

From the results of calculation in section 5.2, it is obvious that the force on a particle chain depends greatly on the assumed positions of particles. We further discuss the approximation of  $\max\{F_x\}$  from  $F_{\alpha 0}$  using equation (12). We have calculated  $\max\{F_x\}$  based on the force  $F_{\alpha 0}$  of isolated chains consisting of two, 32 and an infinite number of particles. Note that the calculation for the isolated chain in figure 16 differs from that for the arrangements in figure 4, as there is no electrode involved and the calculation reduces to an axisymmetrical one (since  $\alpha = 0$ ). Table 1 shows the results of the calculation. As already mentioned, for a finite number (two and 32) of particles,  $F_{\alpha 0}$  is the force acting on the particles at the chain terminals. For an infinite number of particles,  $F_{\alpha 0}$ is determined as the force on the upper or lower half of the particle. The reason why chains of more than two particles are considered here is that, by the method of images, the arrangements in figure 4 may be approximated to arrangements of an infinite number of particles under a uniform field  $E_0$ . By the method of images, if  $\alpha = 0$ , the particle chain in figure 4 is simply vertical, and the net force on any particle is zero. If  $\alpha \neq 0$ , the particle chain still comprises an infinite number of particles, but the chain is no more a straight line. Additionally, there may exist gaps between adjacent particles in the chain.

It can be seen from table 1 that the force depends greatly on the chain model. The two-particle chain gives the lowest value of  $\max\{F_x\}$  for each  $\Gamma_{\varepsilon}$ . The 32-particle chain represents the saturation values of  $\max\{F_x\}$  when the particle number is large. The difference between the force for the two-particle chain and its corresponding saturation value is greater for higher  $\Gamma_{\varepsilon}$ .

Table 2.  $\max\{F_x\}/F_0$  for the arrangements of figure 4.

	Γε			
Figure	4	8	12	
4(a)	2.38	7.53	12.8	
4(b)	4.55	18.5	38.3	
4(c)	2.86	9.24	15.7	
4(d)	4.70	19.9	42.3	

The magnitudes of  $\max\{F_x\}$  obtained for the chain having an infinite number of particles in table 1 are significantly higher than those obtained using the other models. This means that, even where a chain comprises a large number of particles, the model of the infinite particle number may not give the appropriate value of the force on the chain terminals.

Table 2 presents  $\max\{F_x\}$  from our calculation in section 5.2. The forces in table 2 are determined as the maximum of  $F_x$  that are obtained for the range  $0^\circ < \alpha \le 45^\circ$ . For the arrangements of figures 4(b) and (d),  $\max\{F_x\}$  increases with the permittivity ratios roughly by a  $(\Gamma_\varepsilon - 1)^{1.7}$  dependence. As can be seen from tables 1 and 2, none of the isolated-chain models gives the appropriate  $\max\{F_x\}$  for all  $\Gamma_\varepsilon$ . Even though the two-particle chain approximates  $\max\{F_x\}$  comparatively well for the arrangements of figures 4(a) and (c) at low  $\Gamma_\varepsilon$ , the difference becomes fairly high at  $\Gamma_\varepsilon = 12$ . For all the chain arrangements considered here, the approximation from the chain of an infinite number of particles gives force magnitudes higher than those of the results of calculation in table 2, although the difference from  $\max\{F_x\}$  in the arrangement of figure 4(d) decreases with increasing  $\Gamma_\varepsilon$ .

## 6. Conclusions

We have calculated the electric field and dielectrophoretic force on a two-particle chain between parallel-plate electrodes using an analytical method. The calculation has been carried out in three-dimensional conditions, which fully include the effect of the electrodes, for various geometrical arrangements of the particle chain. The results of the calculation show that the electric field intensification and the force significantly increase with the ratio of the particle permittivity to the surrounding (liquid) permittivity. The maximal electric field located at the contact point can be approximated by a very simple formula. The dielectrophoretic force on the chain depends greatly on the spatial deformation of particles in the chain. However, the horizontal force on the upper particle always has a direction opposite to the shear direction. Depending on the chain arrangement, the tilt angle that gives the maximal horizontal force on the upper particle may vary greatly with the permittivity ratio. We have found that it is not sufficient to approximate the maximal horizontal force using the isolatedchain model since no approximation agrees with our results for all the permittivity ratios. The approximation using a chain of an infinite number of particles gives forces that are higher than our results, especially at low permittivity ratios.

### Acknowledgments

This work was supported by the Thailand Research Fund and Ministry of University Affairs.

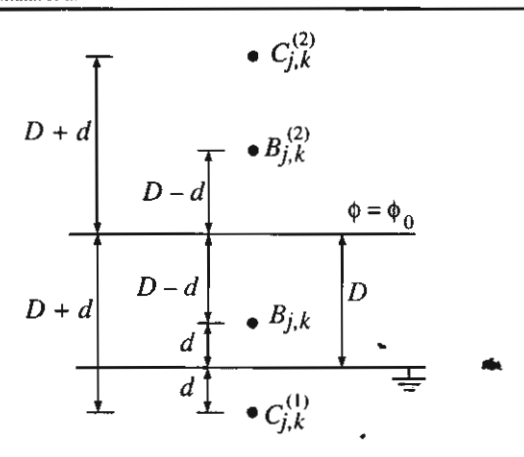


Figure A1. Images of the multipole  $B_{j,k}$  with two parallel plates.

## **Appendix**

This appendix explains how to determine the solutions of the potential for arrangements having more than one electrode. Consider a multipole  $B_{j,k}$  located between two parallel-plate electrodes, as shown in figure A1. Assume that the potentials at the upper and lower electrodes are  $\phi_0$  and zero, respectively. The electrode separation is D.  $B_{j,k}$  is located at a distance d above the lower plate.

The calculation procedure starts with expanding the (undisturbed) potential,  $\phi_{\rm E0}$ , due to the plate electrodes as

$$\phi_{E0} = \frac{d}{D}\phi_0 + \frac{\phi_0}{D}r_B\cos(\theta_B), \tag{A1}$$

which is of the form

$$\phi_{E0} = M_{0,0} + M_{1,0} r_B \bar{P}_{1,0} (\cos \theta_B), \tag{A2}$$

where  $(r_B, \theta_B, \varphi_B)$  are the spherical coordinates in which the position of  $B_{j,k}$  is taken as the origin. If we add the multipole potential to  $\phi_{E0}$ , we obtain

$$\phi^{(0)} = \phi_{E0} + \frac{B_{j,k}}{r_B^{j+1}} \bar{P}_{j,k}(\cos \theta_B) \exp(ik\varphi_B). \tag{A3}$$

The potential  $\phi^{(0)}$  conforms to Poisson's equation, but does not satisfy the potential conditions on the electrodes. Therefore, in the following steps, we place the proper multipole images to satisfy the boundary conditions on the electrodes.

(i) Insert an image multipole  $C_{j,k}^{(1)} = (-1)^{j+k+1}B_{j,k}$  at the same distance, d, below the lower electrode [9]. The potential then becomes

$$\phi^{(1)} = \phi^{(0)} + \frac{C_{j,k}^{(1)}}{r_{C_0}^{j+1}} \tilde{P}_{j,k}(\cos\theta_{C_0}) \exp(ik\varphi_{C_0}), \quad (A4)$$

where  $(r_{C0}, \theta_{C0}, \varphi_{C0})$  are defined in a similar manner as  $(r_B, \theta_B, \varphi_B)$ . The potential  $\phi^{(1)}$  satisfies the zero-potential condition on the lower electrode.

condition on the lower electrode.

(ii) Insert  $B_{j,k}^{(2)}$  and  $C_{j,k}^{(2)}$  as the images of  $B_{j,k}$  and  $C_{j,k}^{(1)}$ , respectively. As in step (i), the images are related to their corresponding multipoles by

$$B_{j,k}^{(2)} = (-1)^{j+k+1} B_{j,k}$$

and

$$C_{j,k}^{(2)} = (-1)^{j+k+1} C_{j,k}^{(1)}$$

The potential is now expressed as

$$\phi^{(2)} = \phi^{(1)} + \frac{B_{j,k}^{(2)}}{r_{j+1}^{j+1}} \bar{P}_{j,k}(\cos\theta_{B2}) \exp(ik\varphi_{B2}) + \frac{C_{j,k}^{(2)}}{r_{C2}^{j+1}} \bar{P}_{j,k}(\cos\theta_{C2}) \exp(ik\varphi_{C2}). \tag{A5}$$

Note that the potential  $\phi^{(2)}$  satisfies the boundary condition on the upper electrode, but the potential on the lower electrode now deviates from zero because of the insertion of  $B_{ijk}^{(2)}$  and  $C_{ijk}^{(2)}$ .

of  $B_{j,k}^{(2)}$  and  $C_{j,k}^{(2)}$ .

(iii) As in the two previous steps, we satisfy the boundary condition repetitively on each electrode. Although the magnitudes of  $B_{j,k}^{(i)}$  and  $C_{j,k}^{(i)}$  do not decrease in the iteration, the positions of the image multipoles consistently become farther from the electrodes. Therefore, we can terminate the iteration when their effects on the plate potential are sufficiently small.

### References

- [1] Jordan T C and Shaw M T 1989 IEEE Trans. Electr. Insul. 24 849–78
- [2] Inoue A, Ryu U and Nishimura S 2001 Proc. 8th Int. Conf. on Electrorheological Fluids and Magnetorheological Suspensions (Singapore: World Scientific) pp 24-9
- [3] Furusho J, Sakaguchi M, Takesue N and Koyanagi K 2001 Proc. 8th Int. Conf. on Electrorheological Fluids and Magnetorheological Suspensions (Singapore: World Scientific) pp 57-62
- [4] Choi Y T and Wereley N M 2001 Proc. 8th Int. Conf. on Electrorheological Fluids and Magnetorheological Suspensions (Singapore: World Scientific) pp 111-17
- [5] Davis L C 1997 J. Appl. Phys. 81 1985-90
- [6] Gonon P et al 1999 J. Appl. Phys. 86 7160-9
- [7] Wu C W and Conrad H 1997 J. Appl. Phys. 81 383-9
- [8] Wu C W and Conrad H 1997 J. Appl. Phys. 81 8057–63
- [9] Techaumnat B, Eua-arporn B and Takuma T 2004 J. Appl. Phys. 95 1586–93
- [10] Jones T B 1995 Electromechanics of Particles (Cambridge: Cambridge University Press)
- [11] Griffiths D J 1989 Introduction to Electrodynamics (Englewood Cliffs, NJ: Prentice-Hall)
- [12] Techaumnat B and Takuma T 2003 IEEE Trans. Dielectric Electr. Insul. 10 623-33
- [13] Takuma T 1991 IEEE Trans. Electr. Insul. 26 500-9

## Calculation of Electric Field and Force on Conductor Particles With a Surface Film

Boonchai Techaumant<sup>1</sup>, Member, IEEE and Tadasu Takuma<sup>2</sup>, Fellow, IEEE

Department of Electrical Engineering, Chulalongkorn University, Phyathai road, Pathumwan, Bangkok, Thailand <sup>2</sup>Central Research Institute of Electric Power Industry, Tokyo, Japan, and also with the Tokyo Denki University, Tokyo, Japan

This paper applies the method of images, an analytical method, to calculate electric field on conductor particles with a surface film. The method utilizes the multipole re-expansion and appropriate fundamental solutions. Electric field is repetitively calculated so as to satisfy all the boundary conditions. The main advantage over flumerical field-calculation methods is that high accuracy can be realized as neither approximation nor discretization of the particle surface or the film thickness is involved. The calculation results for arrangements of a particle chain under a uniform field show the field intensification due to the film thickness and electrical properties. We have also carried out field calculation by the boundary element method (BEM), and compared the results with the analytical ones. The results by the BEM exhibit higher error with decreasing film thickness. Force and yield stress have been calculated from the electric field and compared with experimental results. The comparison shows a good agreement for the ac field, but significant difference for the dc one.

Index Terms-Dielectrophoretic force, electric field, electrorheological (ER) fluid, method of images, particle, surface film.

### I. INTRODUCTION

THE analysis of electric field and dielectrophoretic force is ne of the important topics in many applications of dielectric materials. For example, electrostatic force is a key factor in the behavior of the electrorheological (ER) fluid. The fluid is a suspension of micrometer-size solid particles in a host dielectric liquid [1]. With an application of electric field in the order of MV/m, induced force on particles attracts them to each other, and forms particle chains parallel to the applied field. As a consequence of the chain formation, the fluid exhibits a fast, reversible change in its apparent viscosity. The ER fluid has been proposed for a variety of applications such as the hydraulic valve, clutch, and shock absorber.

Various kinds of particles have been proposed to improve rheological properties of the fluid. In practice, we may classify the particles into three categories: homogeneous particle without any surface element [2], conductor particle with a semi-conducive surface film [3], [4], and insulating particle with a conductive surface film [5]. Up to now, the force behavior of ER fluids having homogeneous particles has been well studied by using the analytical methods [6]-[8], numerical methods [9], [10], and an approximation method including the effects of nonlinear conductivity [2]. By contrast, the behavior of ER fluids having particles with a surface is still unclear. The electric field and force have been analyzed only by using analytical methods in which some approximations on the electric field distribution are applied [4], [11].

In this paper, we apply the method of images to calculate electric field on spherical particles composed of a conductor core and a surface film. The method, using the multipole re-expansion and fundamental solutions of potential, enables us to obtain results of high accuracy. For particles with a thin film, it is generally difficult to realize high accuracy by numerical field calculation methods due to the small film-thickness. A surface

film on the conductor core cannot be simplified by reducing it to a zero-thickness element and applying the condition of surface current [12], since potential gradient is zero on the conductor core. Furthermore, electric field enhancement near a contact point between particles also presents additional calculation difficulty.

### II. CALCULATION ARRANGEMENT

The calculation arrangement is a chain of N spherical particles lying parallel to a uniform external field E0. Fig. 1 shows the calculation arrangement where N=2. Each particle is composed of a conductor core and a semi-conductive surface film. We shall refer to the particle as a conductor-core particle hereafter. Symbols  $\sigma_{\rm F}$  and  $\epsilon_{\rm F}$  represent the film conductivity and permittivity, respectively; while  $\sigma_E$  and  $\epsilon_E$  represent those of the background medium. The particle radius, core radius, and film thickness are denoted by  $R_P$ ,  $R_C$ , and t, respectively. We define a radius ratio  $\zeta$  by  $\zeta = R_{\rm C}/R_{\rm P}$ .

## III. CALCULATION METHOD

A. Re-Expansion of Potential Due to Sources Outside a

Consider a unit multipole of orders  $(n, m), -n \leq m \leq n$ , located at the point q and a particle centered at p in Fig. 2. The multipole potential  $\phi_{\mathbf{B}}^{q}$  is expressed as

$$\phi_{\rm B}^q = \frac{1}{r_q^{n+1}} \tilde{P}_{n,|m|}(\cos \theta_q) e^{\mathrm{i}m\psi_q} \tag{1}$$

where  $(r_q, heta_q, \psi_q)$  are the spherical coordinates where  ${f q}$  is taken as the origin,  $\mathbf{i} = \sqrt{-1}$ , and  $\bar{P}_{j,|k|}$  is the associated Legendre function normalized by  $\sqrt{(n-|m|)!/(n+|m|)!}$ . We shall re-expand the potential  $\phi_{\mathbf{B}}^q$  about the particle center

p, and rewrite the potential as  $\phi_{M}^{p}$  in the following form:

$$\phi_{M}^{p} = \sum_{j=0}^{\infty} \sum_{k=-j}^{j} M_{j,k}^{p} r_{p}^{j} \bar{P}_{j,|k|}(\cos \theta_{p}) e^{ik\psi_{p}}$$
 (2)



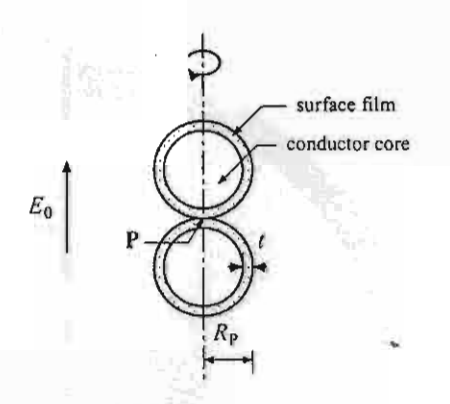


Fig. 1. Calculation arrangement. A chain of particles is lying parallel to a uniform field  $\mathbf{E}_0$ .

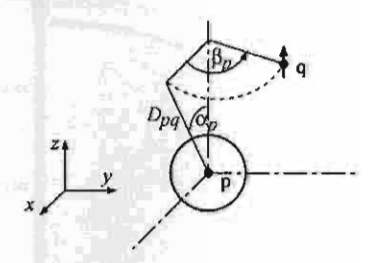


Fig. 2. Multipole at q and a particle centered at p.

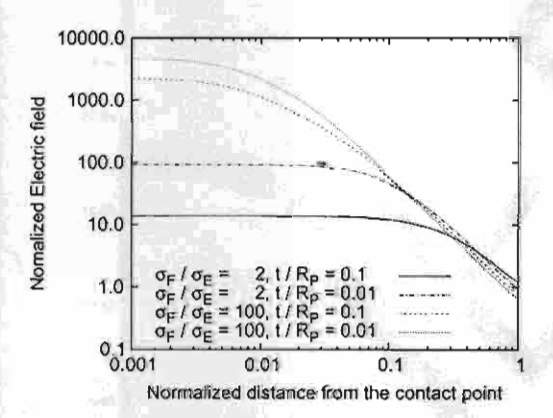


Fig. 3. Normalized electric field in the middle plane between the particles. The abscissa and ordinate are normalized by  $R_{\theta}$  and  $E_{0}$ , respectively.

for  $r_{\rm p} < D_{pq}$ , where the re-expansion moment is given by

$$M_{j,k}^{p} = (-1)^{j} \frac{A_{n,m,j,k}}{D_{pq}^{j+n+1}} \bar{P}_{n+j,|m-k|}(\cos \alpha_{p}) e^{i(m-k)\beta_{p}}$$

....

$$A_{n,m,j,k} = i^{|k-m|-|k|-|m|} \times \sqrt{\frac{(n+m+j-k)!(n-m+j+k)!}{(n+m)!(j-k)!(n-m)!(j+k)!}}.$$

Note that, in (2) the potential due to the source (multipole) outside the particle is now rewritten as a local expansion around the particle center.

For our special case in Fig. 1 where  $E_0 = E_0 a_z$ , we still re-expand the potential in the form of (2) in which  $M_{0,0}^p =$ 

 $-\mathbf{E}_0 \cdot (\mathbf{p} - \mathbf{c}_0), M_{1,0}^p = E_0$ , and  $M_{j,k}^p = 0$  for the other (j,k), where  $\mathbf{c}_0$  is the reference point of zero potential. That is

$$\phi_{M}^{p} = M_{0,0}^{p} + M_{1,0}^{p} r_{p} \tilde{P}_{1,0}(\cos \theta_{p}). \tag{4}$$

B. Fundamental Solutions for a Particle Composed of a Conductor and a Surface Film

Consider a conductor-core particle centered at q lying under an external field which its potential can be written in the form of (2). The resultant potentials  $\phi_F^p$  inside the film and  $\phi_E^p$  in the exterior of the particle can be expressed as

$$\phi_{\rm F}^{p} = \sum_{j=0}^{\infty} \sum_{k=-j}^{j} \left[ N_{j,k}^{p} r_{p}^{j} + \frac{O_{j,k}^{p}}{r_{p}^{j+1}} \right] \bar{P}_{j,|k|}(\cos \theta_{p}) e^{ik\psi_{p}}$$
 (5)

$$\phi_{\rm E}^{p} = \sum_{j=0}^{\infty} \sum_{k=-j}^{j} \frac{B_{j,k}^{p}}{r_{p}^{j+1}} \bar{P}_{j,|k|}(\cos \theta_{p}) e^{ik\psi_{p}} + \phi_{\rm M}^{p}$$

$$= \phi_{\rm B}^{p} + \phi_{\rm M}^{p}$$
(6)

where  $B_{j,k}^p$ ,  $N_{j,k}^p$ , and  $O_{j,k}^p$  are the coefficients to be determined to fulfill the boundary conditions on the core and the film. From the condition of zero total-charge, it can be deduced that  $N_{0,0}^p = M_{0,0}^p$  and  $O_{0,0}^p = B_{0,0}^p = 0$ . The relations between  $M_{j,k}$  and the other potential coefficients for  $j \ge 1$  are given by the following:

$$B_{j,k}^{p} = \frac{C_{1j}K_{E} - C_{2j}K_{F}}{C_{3j}K_{E} + C_{2j}K_{F}}R^{2j+1}M_{j,k}^{p}$$
 (7)

$$N_{j,k}^{p} = \frac{(2j+1)K_{\rm E}}{C_{3j}K_{\rm E} + C_{2j}K_{\rm F}} M_{j,k}^{p}$$
 (8)

$$O_{j,k}^{p} = -R_{C}^{2j+1} N_{j,k}^{p} \tag{9}$$

where the material constants are defined by  $K = \sigma + i\omega\epsilon$ ,  $\omega$  the angular frequency of  $E_0$ , and

$$C_{1j} = j(1 - \zeta^{2j+1}),$$
  
 $C_{2j} = j + (j+1)\zeta^{2j+1},$   
 $C_{3j} = (j+1)(1 - \zeta^{2j+1}).$ 

Note that the potentials are given here for general three-dimensional cases. If a calculation arrangement is axisymmetrical as in Fig. 1, all the coefficients vanish for  $k \neq 0$ , and the expressions of potentials can be simplified.

## C. Calculation Procedure

The solutions of  $\phi_F$  and  $\phi_E$  for the particles in Fig. 1 are obtained by the following repetitive steps.

For each particle, satisfy the initial potential due to E<sub>0</sub> with (4)

$$\phi_{\rm E}^p = (\phi_{\rm M}^p)^{(0)}$$
 for  $p = 1$  to  $N$ .

The superscript (0) denotes the step of repetition.

 Apply the fundamental solutions (5) and (6), and adjust the potentials as follows.

$$\phi_{\rm E}^p = (\phi_{\rm M}^p)^{(0)} + (\phi_{\rm B}^p)^{(0)}$$

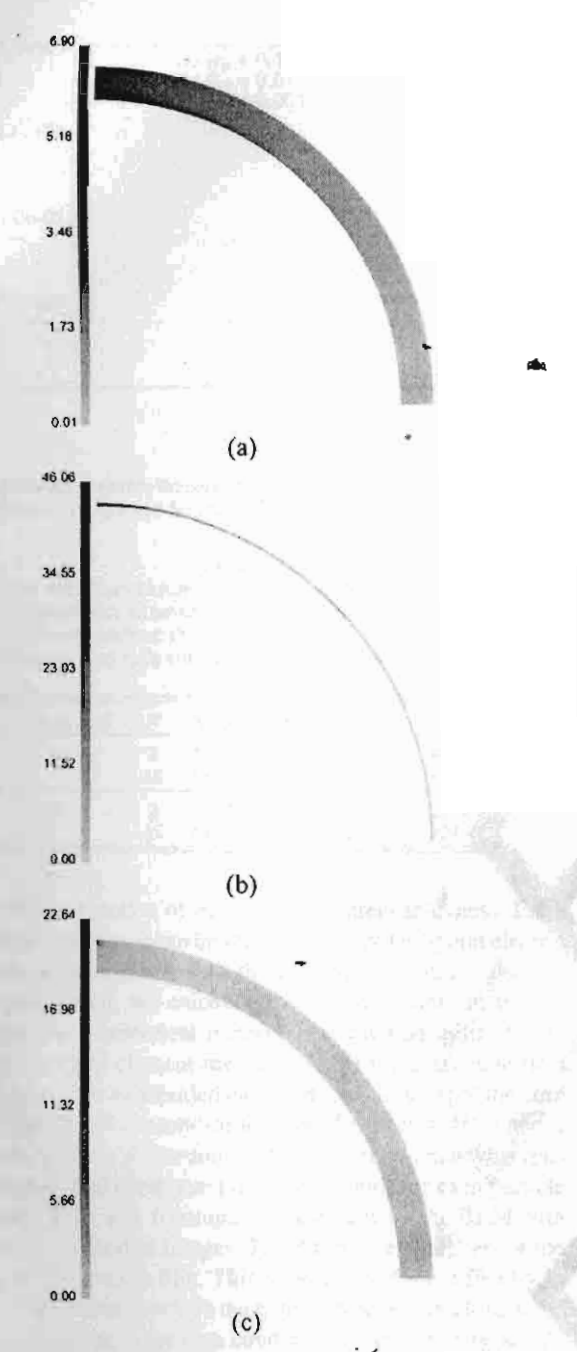


Fig. 4. Normalized electric field inside the surface film on the lower particle. (a)  $\sigma_{\rm F}/\sigma_{\rm E}=2$  and  $t/R_{\rm P}=0.1$ , (b)  $\sigma_{\rm F}/\sigma_{\rm E}=2$  and  $t/R_{\rm P}=0.01$ . (c)  $\sigma_{\rm F}/\sigma_{\rm E}=100$  and  $t/R_{\rm P}=0.1$ .

$$\phi_{\rm F}^p = (\phi_{\rm F}^p)^{(0)}$$

where the potential coefficients are calculated from  $M_{j,k}^p$  by using (7) to (9).

3) For each particle p, using (2), re-expand  $(\phi_B^q)^{(i)}$  obtained in the previous step to  $(\phi_M^p)^{(i+1)}$  for all  $q \neq p$ . Note that  $(\phi_B^q)^{(i)}$  is the potential due to charges (or multipoles) located outside the particle q.

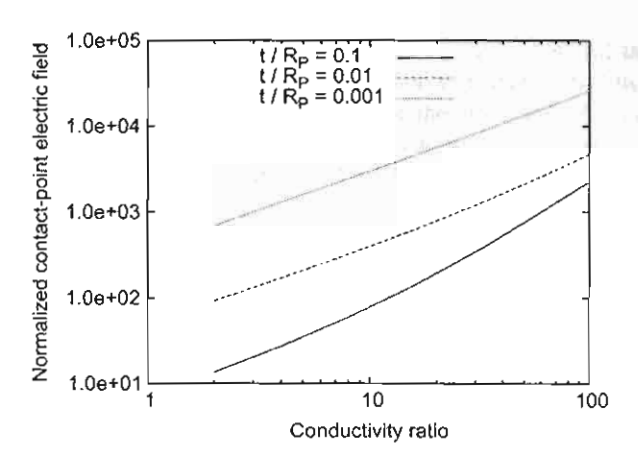


Fig. 5. Normalized electric field at the contact point as a function of  $\sigma_F/\sigma_E$ .

4) Similarly to the second step, rewrite the potentials as

$$\begin{aligned} \phi_{\rm E}^p &= \sum_{n=0}^{i+1} \left[ \left( \phi_{\rm M}^p \right)^{(n)} + \left( \phi_{\rm M}^p \right)^{(n)} \right] \\ \phi_{\rm F}^p &= \sum_{n=0}^{i+1} \left( \phi_{\rm F}^p \right)^{(n)}. \end{aligned}$$

 Repeat Steps 3 and 4 until the solutions of all particles converge.

Although the calculation procedure is described for the arrangement in Fig. 1, it is worth noting that the method presented here can be applied for arbitrary arrangements of conductor-core particles by using a similar procedure [8].

## IV. CALCULATION RESULTS

### A. Electric Field Distribution

We applied the calculation method in Section III to calculate electric field in the arrangement of Fig. 1 for N=2. The calculation parameters were: t=0.1 to 0.001,  $\sigma_{\rm F}/\sigma_{\rm E}=2$  to 100, and  $\omega=0$  (dc field). We used 200 to 2000 expansion terms for potentials, depending on the field nonuniformity. The calculation was terminated when the maximal electric field on particle surface varied less than  $10^{-5}\%$  from the previous iteration step.

Fig. 3 shows the field on the mid-plane between the particles as a function of the distance from P for  $\sigma_{\rm F}/\sigma_{\rm E}=2$  and 100. The field is normalized by  $E_0$ . It can be seen from the figure that the electric field becomes more intensified and nonuniform near the contact point with decreasing the film thickness or increasing the film conductivity.

Fig. 4 shows the field distribution inside the surface film on the lower particle for different film parameters. The effect of t on the electric field in the film is similar to that in Fig. 3, as the field in Fig. 4(b) is more intensified than that in Fig. 4(a). Fig. 4(c) displays the effect of  $\sigma_F$  on the field distribution. With the increase of  $\sigma_F/\sigma_E$  from 2 to 100, the field becomes highly nonuniform near the contact point. This leads to the difficulty for numerical field calculation method to realize high accuracy in the arrangement. Fig. 5 summarizes the contact-point electric

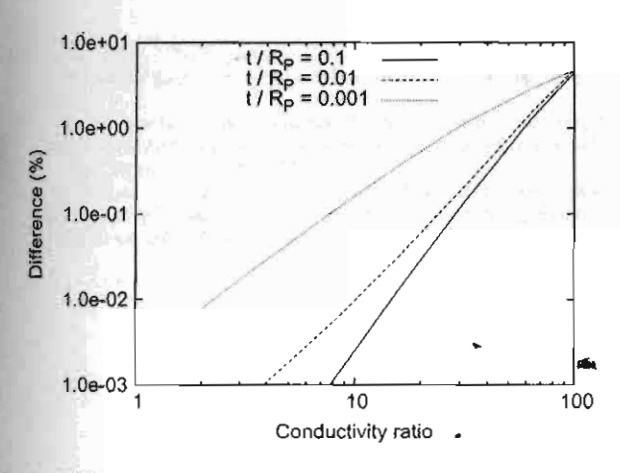


Fig. 6. Difference between the contact-point electric field by the BEM and that by the method of images as a function of  $\sigma_F/\sigma_E$ .

TABLE I

RESULTS OF THE CALCULATION USING PARAMETERS OF A REAL ER FLUID BASED ON DIFFERENT NUMBERS N OF PARTICLES IN A CHAIN.  $E_c$  IS THE CONTACT-POINT ELECTRIC FIELD,  $F_0$  THE FORCE ACTING AT THE CHAIN TERMINAL, AND Ty IS THE SHEAR YIELD STRESS OF THE FLUID.

Applied field	N	$E_{\rm c}/E_{\rm 0}$	$F_0/(\epsilon_0 E_0^2 R_{\mathrm{P}}^2)$	τ <sub>y</sub> (Pa)
ac	2	51.034	167.35	413.56
	16	73.046	353.69	874.05
dc	2	43.511	143.51	354.65
	16	61.364	295.36	729.91

field at P as a function of  $\sigma_F/\sigma_E$  for different thickness. For a sufficiently thin film, it can be seen that the contact-point electric field varies exponentially with the conductivity ratio.

For comparison, we calculated the electric field in the arrangement by a numerical method. The method utilized here was the boundary element method (BEM) for axisymmetrical arrangements. We subdivided each surface (contour) of the core and the film into 512 second-order curved elements (1025 nodes for  $\theta = 0$  to 180°). Accordingly, the number of unknowns (potential and normal component of electric field) for each particle was totally 3076. Fig. 6 compares the results by the BEM with those by the method of images. The difference is higher for the particle with a thinner film. This is because of the difficulty in numerical quadratures where the core surface is very close to the film one. However, at the high conductivity ratio,  $\sigma_F/\sigma_E \approx 100$ in the figure, the difference is approximately the same for all t. This implies that the error due to conductivity mismatch, which contributes to high nonuniformity of electric field, is predominant over that from the numerical quadratures. The difference can be reduced by using a finer subdivision on the spherical surface; however, too small elements may lead to numerical errors in the evaluation of the elliptic integrals involved.

## B. Force and Shear Yield Stress

We compare the shear yield stress of an ER fluid obtained from our calculation with the experimental results [3]. Parameters of the ER fluid are:  $R_P=10~\mu\mathrm{m}$ ,  $t=0.2~\mu\mathrm{m}$ ,  $\sigma_{\mathrm{F}}=4\times10^{-12}~\mathrm{S/m}$ ,  $\sigma_{\mathrm{E}}=2.4\times10^{-12}~\mathrm{S/m}$ ,  $\epsilon_{\mathrm{F}}=5\epsilon_0$ , and  $\epsilon_{\mathrm{E}}=2.5\epsilon_0$ . The applied field is 3 MV/m, dc, or 50-Hz ac. Note that, at the 50-Hz frequency, the effect of  $\epsilon$  is predominant over that of  $\sigma$ .

To determine the shear yield stress, we first calculated the field on the particle chain by the method of images. The force  $F_0$  at the chain terminal was then obtained by integrating the Maxwell's stress on particle surface. The shear yield stress  $\tau_v$ was computed from the maximal force perpendicular to the applied field.

$$\begin{split} \tau_{\rm y} &= \max \left\{ \frac{3}{2} K_{\rm v} \frac{F_0 \cos^3 \theta \sin \theta}{\pi R_{\rm P}^2} \right\} \\ &\approx 0.48714 \times K_{\rm v} \frac{F_0}{\pi R_{\rm P}^2} \end{split} \tag{10}$$

where  $\theta$  is the angle between the chain axis and the applied field, and  $K_v$  is the volume fraction of the particles [5]. For the ER fluid under consideration,  $K_v = 0.2$ . Table I summarizes the calculation results. The force  $F_0$  increases with increasing N, but reaches its saturation value for a sufficiently-long chain. The force for N = 16 in the table represents the saturation value. According to [3], the measured yield stress is approximately 500 Pa for ac field and 100 Pa for dc field. The values of yield stress in Table I agree with the experimental data for the ac case, but are much higher for the dc case. This difference is possibly due to the nonlinear  $\sigma_E$ , which depends on electric field, of the real liquid in the experiment.

### V. CONCLUSION

We have presented an analytical method to calculate electric field on conductor particles with a surface film. The method utilizes the multipole re-expansion and fundamental solutions to repetitively calculate electric field until all the boundary conditions are satisfied. Calculation on example arrangements of a particle chain shows the higher degree of field intensification with increasing film conductivity or decreasing film thickness. We have applied the method for determining the force and shear yield stress of an ER fluid, and compared the calculation results with the experimental ones.

#### REFERENCES

- [1] T. C. Jordan and M. T. Shaw, "Progress in electrorheology," IEEE Trans.
- Dielectr. Electr. Insul., vol. 24, pp. 849-878, 1989.
  P. Atten, C. Boissy, and J.-N. Foulc, "The role of conduction in electrorheological fluids: From interaction between particles to structuration of suspensions," J. Electrostat., vol. 40&41, pp. 3-12, 1997.
- [3] L. C. Davis, "The metal-plarticle/insulating oil system: An idel electrorheological fluid," J. Appl. Phys., vol. 73, pp. 680-683, 1993
- [4] C. W. Wu and H. Conrad, "Influence of a surface film on the particles on the electrorheological response," J. Appl. Phys., vol. 81, pp. 383-389,
- [5] P. Gonon, J.-N. Foulc, P. Atten, and C. Boissy, "Particle-particle interactions in electrorheological fluids based on surface conducting particles," J. Appl. Phys., vol. 86, pp. 7160-7169, 1999.
- [6] M. Washizu and T. B. Jones, "Dielectrophoretic interaction of two spherical particles calculated by equivalent multipole-moment method," IEEE Trans. Ind. Appl., vol. 32, pp. 233-242, 1996.
- [7] B. Techaumnat and T. Takuma, "Calculation of the electric field for lined-up spherical dielectric particles," IEEE Trans. Dielectr. Electr. Insul., vol. 10, pp. 623-633, 2003.
- [8] B. Techaumnat, B. Eua-Arporn, and T. Takuma, "Calculation of electric field and dielectrophoretic force on spherical particles in chain," J. Appl. Phys., vol. 95, pp. 1586-1593, 2004.
- [9] B. Liu, S. A. Boggs, and M. T. Shaw, "Electrical properties of anisotropically filled elastomers," IEEE Trans. Dielectr. Electr. Insul., vol. 8, pp. 173-181, 2001.

- [10] L. C. Davis, "Finite-element analysis of particle-particle forces in electro-rheological fluids," Appl. Phys. Lett., vol. 60, pp. 319-321, 1002
- [11] C. W. Wu and H. Conrad, "Influence of a surface film on conducting particles on the electrorheological response with alternating current fields," J. Appl. Phys., vol. 81, p. 8057, 1997.
- [12] A. Nicolas, J. L. Rasolonjanahary, and L. Krahenbuhl, "Computation of electric fields and potential on polluted insulators using a boundary element method," *IEEE Trans. Magn.*, vol. 28, pp. 1473-1476, 1992.
- [13] L. Greengard and V. Rokhlin, "A new version of fast multipole method for the Laplace equation in three dimensions," Acta. Numerica, vol. 6, 1997.

Manuscript received June 8, 2004. This work was supported by the Thailand Research Fund and in part by the Hitachi Scholarship Foundation.

## Field Intensification at the Contact Point between a Conducting Plane and a Spheroid or an Elliptic Cylinder

B. Techaumnat<sup>1\*</sup> and T. Takuma<sup>2,3</sup>

Department of Electrical Engineering, Chulalongkorn University,
 Phyathai Road, Pathumwan, Bangkok 10330, Thailand
 Central Research Institute of Electric Power Industry,
 2-11-1 Iwado kita, Komae-shi, Tokyo 201-8511, Japan
 Tokyo Denki University, 2-2 Kanda-Nishiki-cho, Chiyoda-ku, Tokyo 201-8457, Japan
 \*E-mail: boonchai.t@chula.ac.th

Abstract: This paper presents an analysis of the electric field at the contact point of zero contact angle for different curvature of the dielectric interface near the contact point. The arrangement considered here is a dielectric solid (a spheroid or an elliptic cylinder) standing on a grounded plane under a uniform external field. The electric field has been calculated by using the boundary element method for 2D and AS arrangements. The calculation results show that the contact-point electric field is intensified by either decreasing the aspect ratio a/b of the dielectric solid or increasing the ratio of the material constant of the solid to that of the surrounding medium. Two simple equations are given for estimating the contact-point electric field for a range of the material-constant ratio with the errors less than 6.6%.

## INTRODUCTION

A triple junction or a contact point, the point where three media meet together, exists in many insulation systems. It may be formed, for example, by a dielectric solid utilized as a mechanical support of an electrode or by a particle adhering to an electrode [1]. Figure 1 gives examples of the contact points (p) at the junctions between the dielectric interface and the electrode. The behavior of the electric field at the contact point is very important as the field is often intensified, possibly causing partial discharge or breakdown in the insulation systems.

The contact-point electric field depends strongly on the contact conditions and the electrical properties of the media involved. According to the contact angle  $\theta_c$  that the dielectric interface makes with the conductor, we can group contact points into three categories: (i)  $\theta_c = 90^\circ$ , (ii)  $0^\circ < \theta_c < 90^\circ$ , and (iii)  $\theta_c = 0^\circ$ . For  $\theta_c = 90^\circ$ , the contact-point field may be enhanced by a certain degree but is still finite [2]. For  $0^\circ < \theta_c < 90^\circ$ , the contact-point field is either zero or infinity, depending on the media involved [2,3,4]. For the last category,  $\theta_c = 0^\circ$ , the field is finite but possibly much more intensified than that in the first category. The electric field at zero-angle

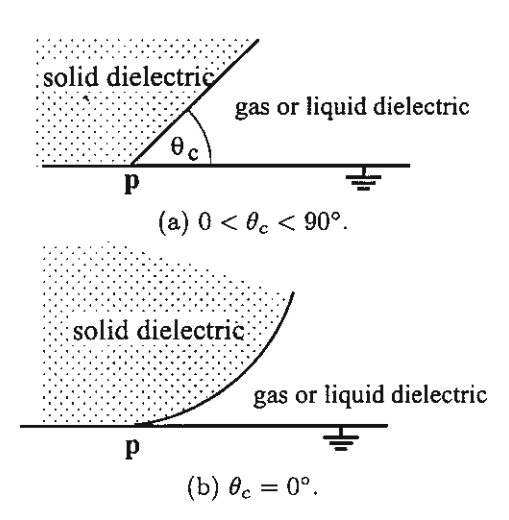


Figure 1: Examples of the contact points.

contact points has been analyzed in [1,5,6,7] but only for the cases where the dielectric interface is circular in cross section near the contact point. However, if we consider the case of particles in an insulation system, it is anticipated that particles thinner than spherical ones may be more deleterious by bringing higher field.

This paper presents an analysis of the electric field at the zero-angle contact point between a conducting plane and a dielectric solid of elliptic cross section. The purpose of the analysis is to clarify how the curvature near the contact point affects the electric field. The electric field has been calculated by using the boundary element method (BEM), a numerical method. The contact conditions treated here is line contact and point contact in the two-dimensional (2D) and axisymmetrical (AS) cases, respectively.

## ARRANGEMENT OF CALCULATION

Figures 2 shows the arrangement of calculation consisting of a dielectric solid standing on a grounded conducting plane under a uniform external field  $\mathbf{E}_0$ . The zero-angle contact point is located at the point

p in the figure. The dielectric solid is an elliptic cylinder in a 2D configuration or a spheroid in an AS configuration. Its geometry is specified by the lengths of the minor and major axes (a and b) as shown in Figure 2. In the calculation, the aspect ratio a/b has been varied from 0.1 to 1.0, while keeping b to be a unit length, to alter the curvature of the dielectric interface near the contact point.

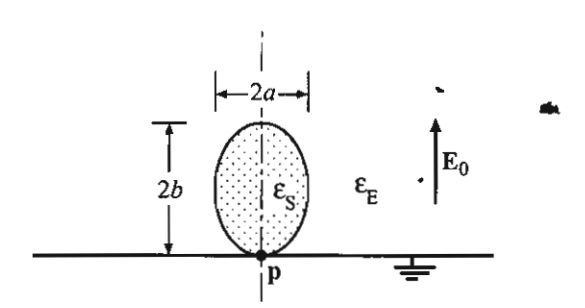


Figure 2: Arrangement of calculation.

As mentioned earlier, the electric field distribution in this arrangement also depends on the material constants of the dielectric solid and the surrounding medium. In a typical insulation system, the material constants are the permittivity  $\varepsilon$  for an ac case or the conductivity  $\sigma$  for a dc case where the surrounding medium is a dielectric liquid. In general, the constants may be represented in a complex form,  $\sigma + j\omega\varepsilon$  or  $\varepsilon - j\sigma/\omega$ , where  $j = \sqrt{-1}$  and  $\omega$  is the angular frequency. For generality, we define  $\Gamma$  as the ratio of the material constant of the dielectric solid to that of the surrounding medium. The field has been calculated for  $\Gamma = 1$  to 32 in this paper. Note that all the material constants are assumed to be constant, independent of the electric field.

## CALCULATION METHOD

The boundary element method (BEM) [8] is utilized to calculate electric field in the arrangement of Figure 2. In the BEM, we subdivide the dielectric interface into elements. At any point  $\mathbf{r}'$  on each element, we express the potential  $\phi(\mathbf{r}')$  as

$$\phi(\mathbf{r}') = \sum N_i^{\phi}(\mathbf{r}')\phi_i \tag{1}$$

and the outward normal component of the electric field  $E_n(\mathbf{r}')$  as

$$E_n(\mathbf{r}') = \sum_i N_i^E(\mathbf{r}') E_{ni}, \qquad (2)$$

where  $N_i^{\phi}$  and  $N_i^{E}$  are the functions interpolating  $\phi$  and  $E_n$  from the nodal values  $\phi_i$  and  $E_{ni}$ , respectively.  $\phi_i$  and  $E_{ni}$  are either defined by the boundary conditions or to be determined by the BEM.

To calculate  $\phi_i$  or  $E_{ni}$ , at each node *i* located at a point **r**, we form a linear equation,

$$C^{\text{int}}(\mathbf{r})\phi_{i} = \int_{S} E_{n}^{\text{int}}(\mathbf{r}')w(\mathbf{r},\mathbf{r}')dS'$$
$$+ \int_{S} \phi(\mathbf{r}')\frac{\partial w(\mathbf{r},\mathbf{r}')}{\partial n}dS'$$
(3)

for the interior of the dielectric solid, or

$$C^{\text{ext}}(\mathbf{r})\phi_{i} = \int_{S} E_{n}^{\text{int}}(\mathbf{r}')w(\mathbf{r},\mathbf{r}')dS'$$

$$+ \int_{S} \phi(\mathbf{r}')\frac{\partial w(\mathbf{r},\mathbf{r}')}{\partial n}dS'$$

$$-\mathbf{E}_{0} \cdot (\mathbf{r} - \mathbf{r}_{0})$$
(4)

for the exterior of the dielectric solid, where w is the fundamental solution of the Laplace's equation, n the outward normal vector at  $\mathbf{r}$ , S the dielectric interface (including its image with respect to the conducting plane), and  $\mathbf{r}_0$  is the reference point of zero potential. The constants  $C^{\mathrm{int}}(\mathbf{r}) = C^{\mathrm{ext}}(\mathbf{r}) = 1/2$  on smooth surface. The superscripts "int" and "ext" in Equation (4) denote the interior and the exterior of the dielectric solid, respectively.

On the interface,  $E_n^{\text{int}}$  is related to  $E_n^{\text{ext}}$  by

$$\Gamma E_n^{\text{int}} + E_n^{\text{ext}} = 0. \tag{5}$$

The fundamental solution w is defined in 2D calculation for  $\mathbf{r}(x,y)$  and  $\mathbf{r}'(x',y')$  as

$$w(\mathbf{r}, \mathbf{r}') = \frac{1}{2\pi} \ln \frac{1}{\sqrt{(x-x')^2 + (y-y')^2}},$$
 (6)

and in AS calculation for  $\mathbf{r}(\rho, z)$  and  $\mathbf{r}'(\rho', z')$  as

$$w(\mathbf{r}, \mathbf{r}') = \frac{K\left(\sqrt{2n/(m+n)}\right)}{\sqrt{m+n}},$$
 (7)

where K is the elliptic integral of the first kind,  $m = \rho^2 + {\rho'}^2 + (z - z')^2$ , and  $n = 2\rho\rho'$ . Equations (3) to (7) are the main equations for the BEM code utilized in this work. To attain high accuracy of the electric field at the contact point, the dielectric interface was subdivided into 720 second-order curved elements.

### RESULTS AND DISCUSSION

The presence of the dielectric solid enhances electric field near the interface even in the absence of the conducting plane. Without the conducting plane, the maximal electric field  $E_{c0}$  in the surrounding medium, located at  $\mathbf{p}$ , is given by [9]

$$\frac{E_{c0}}{E_0} = \Gamma\left(\frac{a/b+1}{\Gamma a/b+1}\right) \tag{8}$$

for the 2D configuration, and

$$\frac{E_{c0}}{E_0} = \frac{\Gamma}{1 + (\Gamma - 1)\alpha} \tag{9}$$

for the AS configuration, where  $\alpha$  is a function of  $\beta = \sqrt{1 - (a/b)^2}$ ,

$$\alpha = \frac{1-\beta^2}{2\beta^3} \left[ \ln \left( \frac{1+\beta}{1-\beta} \right) - 2\beta \right].$$

For reference, Figure 3 presents the values of  $E_{c0}$  where a/b=0.1 to 1.0 and  $\Gamma=4$ , 8, and 12. It is clear that  $E_{c0}$  is intensified by either decreasing a/b or increasing  $\Gamma$ . For a circular cylinder and a sphere (a/b=1.0)  $E_{c0}$  approaches  $2E_0$  and  $3E_0$ , respectively, with  $\Gamma\to\infty$ .

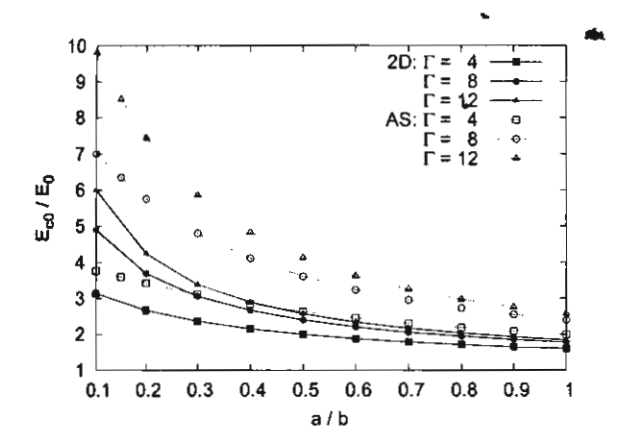


Figure 3: Maximal electric field in the absence of the conducting plane.

With the presence of the conducting plane in Figure 2, the contact-point electric field  $E_c$  (in the exterior) is highly intensified to be significantly greater than  $E_0$ . Figure 4 shows  $E_c$  normalized by  $E_0$  as a function of a/b. As a/b decreases from 1.0, the degree of field intensification increases, and the effect of  $\Gamma$  on the electric field also becomes more significant. It is also implied from Figure 4 that we cannot express  $E_c/E_0$  in a simple form of  $f_1(a/b) \cdot f_2(\Gamma)$ . That is to say the effects on  $E_c$  of a/b and  $\Gamma$  are related to each other. Note that, for the same  $\Gamma$  and a/b, the field is higher in the AS arrangement than in the 2D arrangement.

Figure 5 presents  $E_c$  in relation to  $\Gamma$  for various values of a/b.  $E_c/E_0$  in Figure 5 apparently increases with  $\Gamma$  as an exponential function; however, the slope of each line is not constant throughout the plot. For practical gas-insulated systems under an ac field,  $\Gamma$  should range from 2 to 8. We may estimate the contact-point electric field for a range  $1 \leq \Gamma \leq 8$  using the following expression:

For the 2D configuration,

$$\frac{E_c}{E_0} = \Gamma^k,\tag{10}$$

and for the AS configuration,

$$\frac{E_c}{E_0} = \frac{1}{2}\Gamma(\Gamma^{k-1} + 1),\tag{11}$$

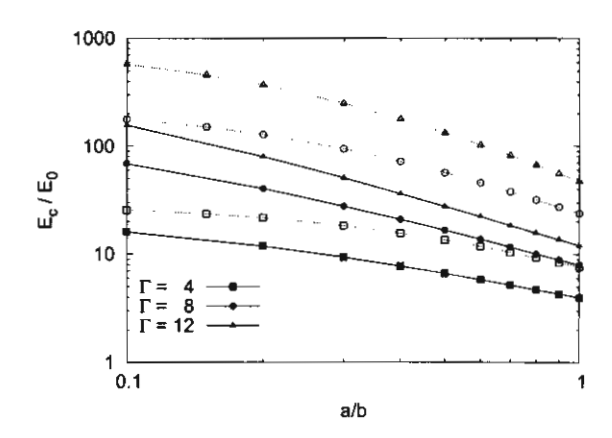


Figure 4: Contact-point electric field as a function of the aspect ratio a/b. The 2D and AS cases are presented with the solid and dotted lines, respectively.

where k is the constant which can be numerically determined. The approximation by Equation (11) was previously proposed for a dielectric sphere (a=b) [2,5]. We obtain k=1.75 here for the sphere whereas in [2,5] k is about 1.77 as the approximation is applied over a slightly wider range of  $\Gamma$  in the references. For a circular cylinder (a=b), it can be derived that k=1 in Equation (10) [10].

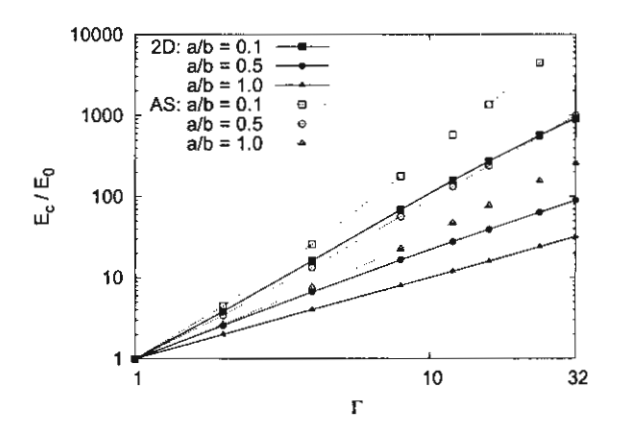


Figure 5: Contact-point electric field as a function of  $\Gamma$ .

Figure 6 compares the electric field estimated using Equation (10) or (11) (the solid or dotted lines) with the results by the BEM (shown by the dots). It is clear that the equations estimate the electric field well for a dielectric elliptic cylinder and a dielectric spheroid having  $0.1 \le a/b \le 1.0$  and  $1 \le \Gamma \le 8$ . The difference between the approximated values and the BEM results is less than 6.6%.

Figure 7 presents k as a function of the aspect ratio a/b. With decreasing a/b from 1.0 to 0.1, k increases consistently from 1.00 to 2.02 and from 1.75 to 2.80 for the 2D and AS cases, respectively. It was pre-

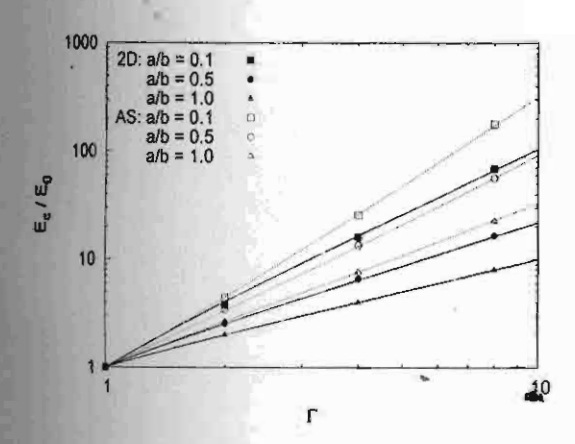


Figure 6: Comparison of the field values from the BEM results (dots) with those from the approximation (lines).

viously suggested that  $k \leq 2$  for a round conductor [2]. However, the results here show that k can be much higher than 2.0 with different curvature near the contact point.

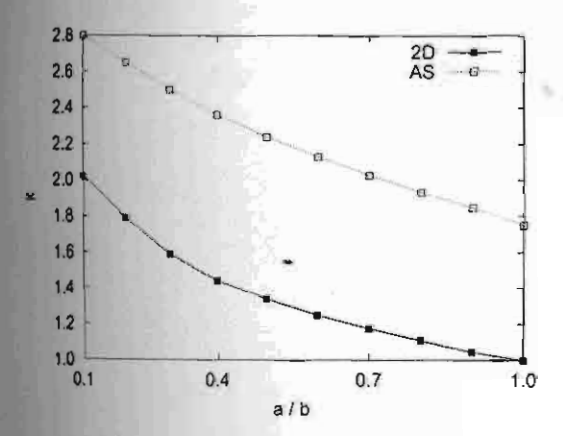


Figure 7: Constant k for approximating the contact-point electric field.

For a higher value of  $\Gamma$ , the contact-point electric field may be simply approximated by the same expression,

$$\frac{E_c}{E_0} \propto \Gamma^k, \tag{12}$$

for both the 2D and AS cases. The constant k for  $\Gamma > 8$  is slightly smaller than that for  $1 \le \Gamma \le 8$  in most cases, except for a/b < 0.2 in the AS arrangement.

### CONCLUSIONS

This paper has analyzed the behavior of the electric at a zero-angle contact point between a conducting plane and a dielectric elliptic cylinder or a dielectric spheroid under a uniform external field. The results can be summarized as follows.

- The contact-point electric field E<sub>c</sub> increases with decreasing the aspect ratio a/b of the dielectric solid or increasing the ratio Γ of the material constant of the dielectric solid to that of the surrounding medium.
- The relation of E<sub>c</sub> to a/b and Γ is complicated and cannot be written as a simple function for the whole ranges of Γ and a/b.
- For 1 ≤ Γ ≤ 8, we may use two simple expressions to estimate E<sub>c</sub> separately for the two-dimensional and axisymmetrical cases with the errors smaller than about 6.6%.
- For a larger value of Γ, E<sub>c</sub> is approximately proportional to Γ<sup>k</sup>.

## ACKNOWLEDGMENT

This work was financially supported by the Thailand Research Fund and in part by the Hitachi Scholarship Foundation.

## REFERENCES

- B. Techaumnat and T. Takuma, Calculation of the electric field for lined-up spherical dielectric particles, IEEE Trans. DEI., Vol.10, No.4, pp.623-633, 2003.
- [2] T. Takuma, "Field behavior at a triple junction in composite dielectric arrangements", IEEE Trans. EI, Vol.26, No.3, June 1991, pp.500-509.
- [3] J. Meixner, "The behavior of electromagnetic fields at edges", IEEE Trans. Antennas and Propagation, Vol.20, No.4, July 1972, pp.442-446.
- [4] B. Techaumnat, S. Hamada, and T. Takuma, "Effect of conductivity in triple-junction problems", Journal of Electrostatics, Vol.56, No.4, pp.67-76, 2002.
- [5] T. Takuma and T. Kawamoto, "Field intensification near various points of contact with a zero contact angle between a solid dielectric and a electrode", IEEE Trans. PAS, Vol.103, No.9, September 1984, pp.2486-2494.
- [6] B. Techaumnat, S. Hamada, and T. Takuma, "Electric field behavior near a zero-angle contact point in the presence of surface conductivity", IEEE Trans. DEI, Vol.9, No.4, pp.537-543, 2002.
- [7] B. Techaumnat, S. Hamada, and T. Takuma, "Electric field behavior near a contact point in the presence of volume conductivity", IEEE Trans. DEI, Vol.8, Nol. 6, pp.930-935, 2001.
- [8] C.A. Brebbia and S. Walker, The boundary element technique in engineering, Butterworths Publishing, 1980.
- [9] P.M. Morse and H. Feshbach, Method of theoretical physics, McGraw-Hill Book Company, 1953.
- [10] T. Takuma and T. Kawamoto, "electric field at various points of contact between rounded dielectric and electrode", 5th Int. Symp. High Voltage Engineering, 33.09, Braunschweig, 1987.